AGU PUBLICATIONS

JGR

Journal of Geophysical Research: Solid Earth

RESEARCH ARTICLE
10.1002/2017JB014226

This article is a companion to Chen and Niemeijer (2017), https://doi.org/10.1002/2017JB014228.

Key Points:
- Physical rationale for the macroscopic frictional strength of a granular fault gouge is given
- Physical interpretations are made for RSF friction parameters *a*, *b*, and D_c
- We provide new scaling relation for critical slip distance D_c with microphysical basis

Supporting Information:
- Supporting Information S1

Correspondence to:
J. Chen,
j.chen3@uu.nl

Citation:
Chen, J., Niemeijer, A. R., & Spiers, C. J. (2017). Microphysically derived expressions for rate-and-state friction parameters, *a*, *b*, and D_c. *Journal of Geophysical Research: Solid Earth*, *122*, 9627–9657. https://doi.org/10.1002/2017JB014226

Received 23 MAR 2017
Accepted 5 OCT 2017
Accepted article online 2 NOV 2017
Published online 4 DEC 2017

©2017. American Geophysical Union. All Rights Reserved.

Microphysically Derived Expressions for Rate-and-State Friction Parameters, *a*, *b*, and D_c

Jianye Chen[1,2], A. R. Niemeijer[1], and Christopher J. Spiers[1]

[1]HPT Laboratory, Department of Earth Sciences, Utrecht University, Netherlands, [2]State Key Laboratory of Earthquake Dynamics, Institute of Geology, China Earthquake Administration, Beijing, China

Abstract Rate-and-state friction (RSF) laws are extensively applied in fault mechanics but have a largely empirical basis reflecting only limited understanding of the underlying physical mechanisms. We recently proposed a microphysical model describing the frictional behavior of a granular fault gouge undergoing deformation in terms of granular flow accompanied by thermally activated creep and intergranular sliding at grain contacts. Numerical solutions reproduced typical experimental results well. Here we extend our model to obtain physically meaningful, analytical expressions for the steady state frictional strength and standard RSF parameters, *a*, *b*, and D_c. The frictional strength contains two components, namely, grain boundary friction and friction due to intergranular dilatation. The expressions obtained for *a* and *b* linearly reflect the rate dependence of these two terms. D_c scales with slip band thickness and varies only slightly with velocity. The values of *a*, *b*, and D_c predicted show quantitative agreement with previous experimental results, and inserting their values into classical RSF laws gives simulated friction behavior that is consistent with the predictions of our numerically implemented model for small departures from steady state. For large velocity steps, the model produces mixed RSF behavior that falls between the Slowness and Slip laws, for example, with an intermediate equivalent slip(-weakening) distance d_0. Our model possesses the interesting property not only that *a* and *b* are velocity dependent but also that D_c and d_0 scale differently from classical RSF models, potentially explaining behaviour seen in many hydrothermal friction experiments and having substantial implications for natural fault friction.

1. Introduction

The rate- and state-dependent friction (RSF) laws were originally developed as a phenomenological description of frictional behavior observed in lab experiments (Dieterich, 1978, 1979; Kato & Tullis, 2001; Linker & Dieterich, 1992; Ruina, 1983). These empirical laws not only explain considerable laboratory data but, in combination with continuum elasticity, have also been extensively applied to explain observed natural and induced fault phenomena (e.g., Marone, 1998; Rice & Ruina, 1983; Scholz, 2002), including earthquake nucleation and rupture propagation (e.g., Ampuero & Rubin, 2008; Dieterich, 1986; Lapusta & Rice, 2003; Rubin & Ampuero, 2005; Tse & Rice, 1986), aftershocks and fault restrengthening following rapid slip (Chen & Lapusta, 2009; Dieterich, 1994; Helmstetter & Shaw, 2009; Marone et al., 1991, 1995), afterslip both within and adjacent to dynamic ruptures (Scholz, 2002; Segall, 2010), and interseismic creep processes (Barbot et al., 2009; Hetland et al., 2010), as well as episodic aseismic deformation transients (also called slow slip events) that have recently been observed in a number of plate boundaries (Hawthorne & Rubin, 2013; Liu & Rice, 2005; Liu & Rubin, 2010; Segall et al., 2010; Shibazaki & Shimamoto, 2007). No other theory allows for such quantitative predictions.

However, these laws are not readily envisioned in terms of the underlying physics (e.g., Baumberger et al., 1999; Beeler et al., 2008; Berthoud et al., 1999; Ikari et al., 2016; Nakatani, 2001; Noda, 2008; Rice et al., 2001; Sleep, 2005). Most work up to now is based on the theory of pure contact creep, which has been widely accepted to be a thermally activated (rate-dependent) process operating on the sliding surfaces (e.g., Baumberger et al., 1999; Beeler et al., 2007; Berthoud et al., 1999; Chester, 1994; Dieterich, 1979; Estrin & Bréchet, 1996; Hatano, 2015; He et al., 2013; Heslot et al., 1994; Nakatani, 2001; Persson, 1998; Putelat et al., 2011; Rice et al., 2001; Sleep, 1997, 2005; Stesky, 1977). A simple form of this approach usually proceeds as follows: assuming higher microscopic stresses on contacts than those nominally applied (Estrin & Bréchet, 1996) and representing frictional sliding as a creeping process that obeys a rheological equation of the exponential form, a final relation can be derived which shows that the *a* value (i.e., the instantaneous response of friction to a change in driving velocity) is proportional to absolute temperature (e.g., Hatano, 2015;

Nakatani, 2001; Rice et al., 2001). A similar relation has also been obtained for the evolution parameter b (He et al., 2013; Ikari et al., 2016; Nakatani & Scholz, 2004; Sleep, 2005). However, the physical processes that operate in gouge-filled fault zones, as revealed by microstructural and micromechanistic studies, are more complicated than pure contact creep, and other mechanisms such as subcritical cracking, cataclastic granular flow (together with grain rolling and comminution), and grain boundary sliding, as well as shear-induced dilatancy, are expected to be active (e.g., Bos & Spiers, 2002; Richardson & Marone, 1999; Segall & Rice, 1995; Sleep, 1995).

In the seismic cycle of natural faults, the range of slip rates involved is large (Scholz, 2002) and it is appealing to describe different regimes using a single friction law. One of the big successes of RSF laws is the logarithmic rate dependence of steady state friction coefficient, typically expressed by $(a - b)$, which can be taken as an indicator of the potential of a fault to exhibit stable versus unstable frictional behavior. However, it has been widely observed that the steady state friction coefficient is not a monotonic function of slip rate but typically increases with slip rates at very low and high slip rates and decreases in between (e.g., Bos & Spiers, 2002; Buijze et al., 2017; Carpenter et al., 2014; den Hartog & Spiers, 2013; Di Toro et al., 2011; Heslot et al., 1994; Ikari et al., 2009; Niemeijer et al., 2016; Reches & Lockner, 2010; Shimamoto, 1986). For instance, by reducing slip rates, Shimamoto (1986) found for halite a transition from a velocity-strengthening frictional regime, via a velocity-weakening frictional regime, and back to a strengthening one in which ductile shear deformation is expected to be active. On the other hand, at very high (seismic) slip rates when frictional heating becomes significant, other weakening effects have been widely observed (Di Toro et al., 2011; Reches & Lockner, 2010). Efforts have been made to incorporate the heating effect at high slip rates into the RSF laws, based on the inferred physical mechanisms in the friction phenomenon (e.g., flash heating and thermal and chemical pressurization, Noda, 2008). However, the variation in friction rate dependence at low slip rates (in the earthquake or slow slip nucleation regime) is not captured or explained by the classical concepts underlying the RSF laws, partially due to the obscurity of the physical mechanisms. Hence, major uncertainties exist when taking constant or variable $(a - b)$ obtained from experiments as an indicator of fault slip stability. To apply the experimentally derived friction laws to natural fault zones and to extrapolate them beyond their experimental conditions, friction models with a microphysical basis are required (e.g., Bos & Spiers, 2002; den Hartog & Spiers, 2014; Ikari et al., 2016; Nakatani, 1998; Niemeijer & Spiers, 2007; Sleep et al., 2000; Sleep, 2005).

Another important parameter in RSF laws is the critical slip distance, D_c, the distance over which a fault loses or regains its frictional strength after a perturbation in the loading conditions (Ida, 1973; Palmer & Rice, 1973), because, in principle, it determines the maximum slip acceleration and radiated energy during an earthquake (e.g., Aki, 1987) insofar that it influences the magnitude and time scale of the associated stress breakdown process (e.g., fracture energy) (Ampuero & Rubin, 2008; Mikumo et al., 2003; Ohnaka, 2003; Rubin & Ampuero, 2005; Scholz, 2002). Regardless of the importance, it is paradoxical that the values of D_c reported in the literature range from a few to tens of microns as determined in typical laboratory experiments with bare surfaces and gouge layers (Dieterich, 1979; Marone, 1998; Scholz, 2002), to 0.1–5 m as determined in numerical and seismological estimates based on geophysical observations (e.g., Ide & Takeo, 1997; Kaneko et al., 2017; Yasuda et al., 2005), and further to several meters as determined in high-velocity laboratory experiments (Di Toro et al., 2011; Niemeijer et al., 2011; Tsutsumi & Shimamoto, 1997). Note that among these studies, the critical length scale parameter in the constitutive friction laws (D_c) may differ from the slip-weakening distance inferred from the traction evolution curves obtained for natural or laboratory faults. The latter, as usually derived from scenarios where perturbations are large (e.g., velocity steps of large magnitudes or tips of dynamic rupture nucleation zones; Ampuero & Rubin, 2008; Bhattacharya & Rubin, 2014; Bizzarri & Cocco, 2003)), is also referred to as the equivalent or effective slip-weakening distance (d_0^{eq} or d_0, see a review by Marone et al., 2009). Moreover, in most numerical simulations of dynamic rupture propagation with prescribed friction laws, D_c is imposed a priori and its value is often assumed to be constant and uniform on the fault plane. Understanding the physics that controls the critical slip distance and explains the gap between observations from experimental and natural faults is thus one of the crucial problems in both the seismology and laboratory communities (Marone & Kilgore, 1993; Ohnaka, 2003).

By using microphysical models established from the inferred deformation mechanisms, some pioneering works have succeeded in predicting the steady state frictional strengths of different fault gouges (Bos & Spiers, 2002; den Hartog & Spiers, 2014; Niemeijer & Spiers, 2007). Recently, Chen and Spiers (2016) developed a more general model based on the one presented by Niemeijer and Spiers (2007), describing both

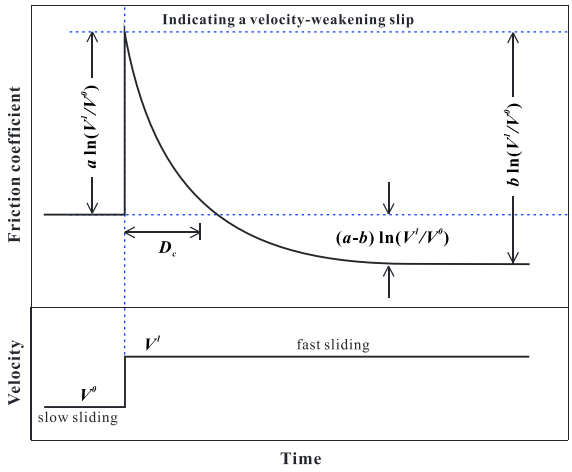

Figure 1. Schematic diagram showing the definition of RSF parameters in a velocity-stepping test.

the steady state and transient frictional behavior of a granular fault gouge (referred to as CNS model from now on). The model was derived using robust properties of granular friction, which therefore is general (and not model specific). By using this model, typical friction experiments can be simulated, namely, "velocity step" (VS) and "slide-hold-slide" tests. The modeling results capture all of the main features and trends observed in the experiments, including both steady state and transient aspects of the observed behavior, with reasonable quantitative agreement (Chen & Spiers, 2016).

In this paper and the companion paper (Chen & Niemeijer, 2017), we extend our model, which we explored only numerically thus far, and obtain analytical solutions for classical RSF parameters from a purely microphysical basis. In the present paper, by analytically solving the constitutive equations under boundary conditions corresponding to a VS test (as done in typical laboratory experiments, and assuming relatively small steps), we obtain theoretical expressions for the RSF parameters, that is, a, b, and D_c, as functions of material properties (e.g., creep rate parameters, solid solubility, and activation volume), microstructural parameters (grain size, porosity, and shear band thickness), and experimental conditions (temperature, effective normal stress, and imposed slip rate). The model predictions are consistent with the lab observations (especially at hydrothermal conditions), in broad agreement with current interpretations of these parameters, and also with the results of the forward RSF modeling performed for small perturbations using parameters calculated with the derived expressions. Finally, we extrapolate the parameters to natural conditions and discuss their implications for natural faults.

2. Constitutive Models

In this section, we describe and compare the RSF law and the CNS model. The RSF law has already been discussed extensively in the literature; our comments on it are brief. We explain the underlying physics of the model and present the constitutive equations in this section.

2.1. Rate- and State-Dependent Friction Laws

The RSF law is a phenomenological law, introduced to capture the experimental observations of both steady state and transient friction (Dieterich, 1979; Ruina, 1983). In RSF laws, the shear stress (τ) of a fault is a function of normal stress (σ_n), sliding rate (V), and state variable (θ). The dependence on both rate and state is logarithmic, expressed as follows:

$$\tau = \tau^* + a\sigma_n \ln\left(\frac{V}{V^*}\right) + b\sigma_n \ln\left(\frac{V^*\theta}{D_c}\right). \tag{1}$$

This equation describes the evolution of shear stress from a steady state value (τ^*) at a reference sliding rate (V^*) and its subsequent evolution toward a new steady state over a critical slip distance (D_c), in response to a perturbation in state (θ) or sliding rate (V). The state variable is thought to represent the average lifetime of grain-to-grain contacts, which can be described by so-called state equations, such as the Dieterich (Slowness) law:

$$\dot{\theta} = 1 - V\theta/D_c \tag{2}$$

and the Ruina (Slip) law:

$$\dot{\theta} = -V\theta/D_c \ln(V\theta/D_c). \tag{3}$$

In these equations, there are three constitutive parameters, namely, the direct effect (a), the evolutional effect (b), and the characteristic (critical) slip distance D_c (Marone, 1998). These, along with the derived parameter, $(a - b)$, specify the intrinsic frictional properties of a gouge material. As shown in Figure 1, the values of these

parameters are usually quantified from friction curves obtained from VS tests. Mathematically, their values can be identified as follows (Rice, 1983):

$$a = \frac{\partial \mu}{\partial(\ln V)}\Big|_{(V=V_{ss},\theta=\theta_{ss})}, \tag{4a}$$

$$(a-b) = \frac{\partial \mu_{ss}}{\partial(\ln V)}\Big|_{V=V_{ss}}, \tag{4b}$$

$$D_c = -\frac{V}{\partial(\mathrm{d}\theta/\mathrm{d}t)/\partial\theta}\Big|_{(V=V_{ss},\theta=\theta_{ss})}. \tag{4c}$$

Here the subscript "ss" denotes steady state. Since the equations given in (4a)–(4c) are derived from a general frictional phenomenon (Rice, 1983), these relations can apply for any rate- and state-dependent friction law, with one or more state variables.

2.2. The Microphysical Model (CNS Model)

The CNS model is developed for granular material based on microstructural observations and the inferred microscopic deformation mechanism(s). In the model, a granular fault gouge is ideally represented by densely packed cylinders or spheres. Since localization has been widely observed in both natural and lab-simulated fault zones, we incorporate a localized shear band, developed at the margin of the bulk gouge (Figure 2a). Both gouge zones, that is, shear band and bulk sample, are characterized by the same pattern of grain packing but with different mean diameters, representing the constituent particles (Figures 2a and 2b). The deformation of the gouge is controlled by parallel processes within each zone, that is, dilatant granular flow plus an arbitrary creep mechanism at grain contacts, for example, intergranular pressure solution (IPS). The present model only considers the frictional phenomenon after the material has reached a constant grain size and thickness of the localized band, which means that deformation mechanisms such as de/localization, cataclasis, microcracking, grain rolling, and comminution are not included at present. Constitutive equations of the CNS model are derived by applying a unified approach to this kinematic, energy-dissipating friction system, that is, momentum and energy/entropy conservation. As given by Chen and Spiers (2016), they are in the original form as follows:

$$V = L_t\left[\lambda\dot{\gamma}_{pl}^{sb} + (1-\lambda)\dot{\gamma}_{pl}^{bulk}\right] + L_t\lambda\dot{\gamma}_{gr}, \tag{5a}$$

$$-\frac{\dot{\varphi}^{sb}}{1-\varphi^{sb}} = \dot{\varepsilon}_{pl}^{sb} + \left(-\dot{\gamma}_{gr}\tan\psi\right), \tag{5b}$$

$$\tau = \frac{\widetilde{\mu} + \tan\psi}{1-\widetilde{\mu}\tan\psi}\sigma_n, \tag{5c}$$

$$\widetilde{\mu} = \widetilde{\mu}^{*} + a_{\widetilde{\mu}}\ln\left(\frac{\dot{\gamma}_{gr}}{\dot{\gamma}_{gr}^{*}}\right). \tag{5d}$$

In these equations, slip localization is specified by a localization degree λ and the total gouge layer thickness L_t. Superscripts "sb" and "bulk" denote the shear band and the bulk gouge, respectively. Subscript "pl" indicates the nonreversible time-dependent creep mechanism at the grain contacts, and "gr" indicates granular flow. Further, $\dot{\gamma}$ and $\dot{\varepsilon}$ indicate the shear and normal strain rates, respectively. Following these definitions, $\dot{\gamma}_{pl}^{sb}$ and $\dot{\gamma}_{pl}^{bulk}$ denote the creep-induced shear strain rates in the shear band and bulk sample, respectively. Equation (5a) expresses the kinematic relation in the shear direction. In the present model, granular flow is assumed to only occur in the shear band such that the bulk shear displacement is attributed to shear creep in the entire sample thickness with the additional granular flow in the shear band (Figure 2c). Equation (5b) expresses the normal strain rate in the shear band (positive for compaction), where φ^{sb} is porosity, $\dot{\varepsilon}_{pl}^{sb}$ is creep-induced compaction rate, and $-\dot{\gamma}_{gr}\tan\psi$ is the dilatational rate induced by intergranular slip (Paterson, 1995). Here ψ is the average dilatation angle of all the interacting grain contacts within the shear zone (Figure 2b) and the negative sign indicates dilatation. Equation (5c) is obtained from the energy/entropy balance approach, expressing the macroscopic shear and normal stresses linked by the dilatation angle and grain

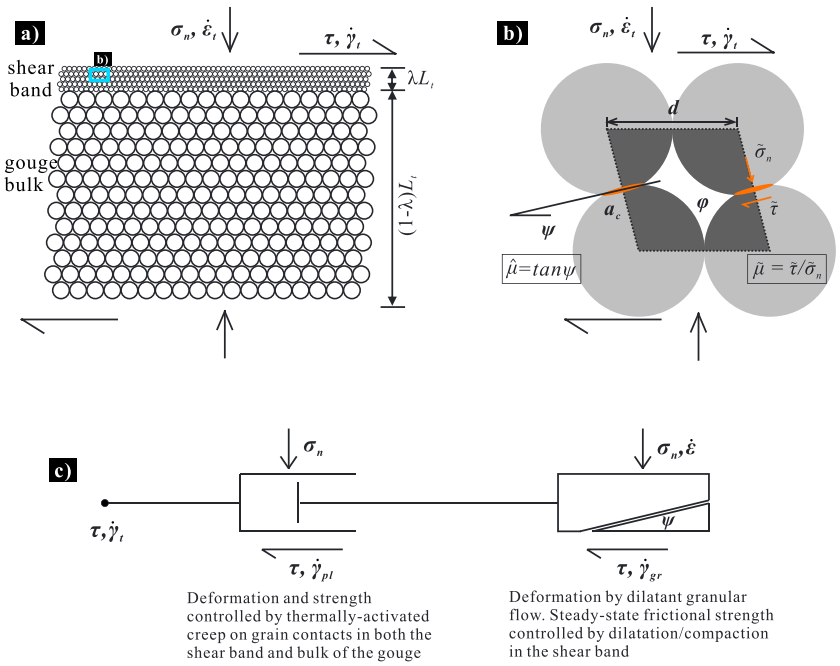

Figure 2. (a) An idealized microstructural model for a simulated fault zone, characterized by a shear band developed at the margin of a bulk gouge layer. The thickness of the shear band is defined as λL_t, where L_t is the total thickness of the gouge layer and λ is taken as a constant defining relative shear band thickness ($\lambda \leq 1$). Both the shear band and the bulk gouge layer are represented by densely packed spheres, with varied mean diameters (d) and compaction states. In the CNS model, the compaction state is controlled by the competing processes, that is, compactional creep at grain contacts versus shear-induced dilatation by granular flow. (b) The unit cell characterizing the grain packing in the present microstructural model, in which the key microstructural state variables, that is, porosity (φ), dilatancy angle (ψ), and contact area (a_c) are illustrated. Note that these variables are average quantities determined over the entire shear zone. For instance, the individual grain contacts can be inclined, horizontal or vertical, but the average contacting angle (ψ value) should be $\geq$0. With the absence of dilatant granular flow in the bulk layer, the ψ value is much larger. The externally applied effective normal and corresponding shear stresses (σ_n and τ) are transmitted across the grain contacts, causing intensified effective normal and shear stresses acting on the contacts ($\tilde{\sigma}_n$ and $\tilde{\tau}$). The imposed shear displacement rates or compaction strain rates ($\dot{\gamma}_t$ and $\dot{\varepsilon}_t$) are accommodated by grain boundary sliding and a contact creep deformation. A cohesion-free slip criterion is used for grain boundary sliding on each contact such that $\tilde{\mu}\equiv\tilde{\tau}/\tilde{\sigma}_n$, where $\tilde{\mu}$ is the grain boundary friction coefficient. The dilatant effect contributes to the frictional strength approximately by tanψ, which is defined as a dilatant friction coefficient that is $\hat{\mu}\equiv$tanψ. (c) Mechanical analog diagram showing that the bulk shear displacement of a granular fault gouge is attributed to shear creep in the entire sample thickness with the additional granular flow in the shear band.

boundary friction ($\tilde{\mu}$). Note that in (5c), we assume a cohesion-free grain boundary slip criterion expressed as $\tilde{\tau} = \tilde{\mu}\tilde{\sigma}_n$, where $\tilde{\tau}$ and $\tilde{\sigma}_n$ are shear and normal stresses on a contact, respectively (Figure 2b). Being derived from a lattice scale (Chen & Spiers, 2016), grain boundary sliding is a generally thermally activated process but distinguished from a specific creep law that accounts for the plastic creep at grain contacts. Accordingly, $\tilde{\mu}$ is intrinsically strain rate strengthening as described in equation (5d), where $a_{\tilde{\mu}}$ is the logarithmic rate dependent coefficient ($a_{\tilde{\mu}} = \dfrac{\partial\tilde{\mu}}{\partial(\ln V)}$) and $\tilde{\mu}^*$ is the reference $\tilde{\mu}$ value at a reference shear strain rate $\dot{\gamma}^*_{gr}$.

The above set of equations comprises the constitutive equations of the model. Substituting (5d) into (5c), the equations can be reformulated as follows:

$$\tau = \frac{\left[\tilde{\mu}^* + a_{\tilde{\mu}}\ln\left(\dot{\gamma}_{gr}/\dot{\gamma}^*_{gr}\right)\right] + \tan\psi}{1 - \left[\tilde{\mu}^* + a_{\tilde{\mu}}\ln\left(\dot{\gamma}_{gr}/\dot{\gamma}^*_{gr}\right)\right]\tan\psi}\sigma_n. \tag{6}$$

Recall that we assume granular flow only to occur in the shear band, and from now on we will drop the superscript sb except where otherwise stated. Equation (6) expresses the shear stress (τ) as a function of normal

stress (σ_n), shear strain rate at grain boundaries ($\dot{\gamma}_{gr}$) and the "state" of the gouge (ψ). Rewriting (5b), the evolution of porosity can be described as a function of shear strain rate ($\dot{\gamma}_{gr}$) and creep-induced compaction strain rate ($\dot{\varepsilon}_{pl}$), which, as given later, depends on σ_n and porosity.

$$\frac{\dot{\varphi}}{(1-\varphi)} = \dot{\gamma}_{gr} \tan\psi - \dot{\varepsilon}_{pl}. \tag{7}$$

Porosity (φ), average dilatancy angle (ψ), and average contact area (a_c) are referred to as the three state variables characterizing the internal microstructural configuration of a granular fault gouge (see their definitions in Figure 2b). Since the present model considers a friction process after the grain size has reached a constant level, these variables are interdependent on one another (one-to-one correspondence), such that the model can be taken as a single state variable system (the linking functions are explained in the next section). It is desirable to express the state in terms of a microphysically observable property and porosity is a natural choice (Nakatani, 1998; Sleep, 1997). As such, equations (6) and (7) can be regarded as the "friction law" and "state law" of the CNS model, respectively.

2.3. Comparison Between RSF Laws and the CNS Model

A comparison of the sets of equations (1) and (2) and (6) and (7) indicates that the classical RSF laws and the microphysical model have several similarities. As addressed above, the key similarity is that they are both rate- and state-dependent and both conform to a single state variable system. Each model has its advantages and disadvantages. Although the establishment of our model was not specifically intended to fix or replace classical RSF laws (Chen & Spiers, 2016), it has the following advantages: (1) The governing equations are rigorously derived and have a fundamental microphysical basis, and the key state variable, that is, porosity, has a microstructurally verifiable meaning (Sleep, 1997; Sleep et al., 2000). (2) Any creep mechanism operating at grain contacts can be incorporated into the model depending on the material and conditions. (3) Effective normal stress (σ_n = externally applied normal stress minus pore pressure) has an active role in the model (through $\dot{\varepsilon}_{pl}$), and therefore, it does not necessitate an additional term (or sensitivity factor) to describe the evolution of shear stress in response to a σ_n change (cf. Linker & Dieterich, 1992). (4) Temperature is embodied in the model as well, and it is expected to influence the friction behavior through affecting either the $a_{\tilde{\mu}}$ value or the contact creep rate via an Arrhenius law. (5) Finally, as velocity decreases, a friction-to-flow transition appears naturally from the model, as will be demonstrated later in this paper.

Disadvantages of the CNS model are also apparent. First, the model composes of cumbersome equations, which cannot be readily applied, as the RSF laws, for numerical simulations of earthquake phenomena. Second, the parametric ingredients of the model include internal microstructures of the studied fault (porosity, grain size, and shear zone thickness), material properties of the granular gouge (e.g., creep law parameters like activation energy, stress sensitivity, and grain size sensitivity), ambient conditions the fault is subjected to (temperature and normal stress), and the constitutive linking relations of different state variables. These parameters are not always well constrained for a reliable extrapolation and implementation of the model. For instance, we have assumed a steady state microstructure, that is, grain size and localized band thickness are not changing. Obviously, this is not always the case under either simulated or natural faulting conditions. Moreover, although the model is plausibly applicable to a gouge-filled fault system, it is not clear whether it can be applied to describe friction of bare rock surfaces.

Finally, it is noteworthy that previous studies have also attempted to link observed laboratory porosity evolution to the classical RSF model (Nakatani, 1998; Segall & Rice, 1995; Sleep, 1995) or the shear transformation zone theory (Daub & Carlson, 2008; Lieou et al., 2017). Our model differs from these models insofar that it ties the frictional behavior to the competition between the dilatation and compaction of the shear zone, which, as explained by equation (7), are each fully microphysically based and attributed to different mechanisms, namely, granular flow and plastic creep at grain contacts.

3. Constant Velocity Sliding and Steady State Friction/Flow

In this and the next sections, we will analytically solve the governing equations of the CNS model under the assumption of two typically employed boundary conditions, namely sliding at a constant velocity and an

abrupt perturbation of the driving velocity. We start with sliding at a constant velocity. At steady state, shear stress is constant ($\dot{\tau} = 0$). The microstructure, hence porosity and dilatation angle, characterizing the gouge material, should also be constant so that $\dot{\varphi} = 0$. Equations (5a)–(5d) will consequently reduce to

$$V_{\text{imp}} = L_t\left[\lambda\dot{\gamma}_{\text{pl}}^{\text{sb}} + (1-\lambda)\dot{\gamma}_{\text{pl}}^{\text{bulk}}\right] + L_t\lambda\dot{\gamma}_{\text{gr}}, \tag{8a}$$

$$\dot{\varepsilon}_{\text{pl}} = \dot{\gamma}_{\text{gr}}\tan\psi_{\text{ss}}, \tag{8b}$$

$$\tau_{\text{ss}} = \frac{\widetilde{\mu}_{\text{ss}} + \tan\psi_{\text{ss}}}{1 - \widetilde{\mu}_{\text{ss}}\tan\psi_{\text{ss}}}\sigma_n, \tag{8c}$$

$$\widetilde{\mu}_{\text{ss}} = \widetilde{\mu}^{*} + a_{\widetilde{\mu}}\ln\left(\frac{\dot{\gamma}_{\text{gr}}}{\dot{\gamma}_{\text{gr}}^{*}}\right). \tag{8d}$$

Equation (8a) indicates that shear displacement is accommodated by two serial processes, that is, the shear component of contact creep and granular flow (Figure 2c). By virtue of their relative contribution, in the following, we will solve these equations for two end-member cases.

3.1. Intermediate-Velocity Friction Regime (With Negligible Shear Creep)

We first assume that the shear component of contact creep is negligibly small, which means the sample shear deformation can be completely attributed to intergranular granular flow ($V_{\text{imp}} = L_t\lambda\dot{\gamma}_{\text{gr}}$). As such, equations (8a) and (8b) can be combined into

$$V_{imp} = \frac{L_t\lambda\dot{\varepsilon}_{pl}}{\tan\psi}. \tag{9}$$

Volumetric strain rate of rocks or aggregates consisting of a single mineral or mineral assemblages can generally be expressed as a function of temperature, mean grain size, and the applied stress in a power and exponential form as follows (Berthoud et al., 1999; Poirier, 1985):

$$\dot{\varepsilon}\equiv E_{\text{pl}}(T,d,\sigma_n) = A_{\text{pl}}\exp\left(-\frac{E_a}{RT}\right)\frac{{\sigma_n}^n}{d^m}, \tag{10a}$$

$$\dot{\varepsilon}\equiv E_{\text{pl}}(T,d,\sigma_n) = A_{\text{pl}}\exp\left(-\frac{E_a}{RT}\right)\exp\left(\frac{\sigma_n\Omega}{RT}\right)\frac{1}{d^m}, \tag{10b}$$

where E_a is activation energy; R, the gas constant; T, absolute temperature (K); d, mean particle size; m, grain size sensitivity factor; n, stress exponent for the creep law; Ω, activation volume, and A_{pl}, a preexponential rate constant. We adopt these general laws to describe creep at the grain contacts. Bear in mind that these laws are commonly derived from rheological experiments that are typically run at high temperature and pressure conditions, where the deforming material tends to be compacted and have a relatively low porosity (<5%). However, in a dynamic friction process, a granular material tends to be more porous and can dilate volumetrically to allow particles to slide, roll, and rearrange and thus accommodate shear displacement. Consequently, the local stresses transmitted across the grain contacts could be much higher than the macroscopic ones that are either nominally applied to or externally measured from the system. Therefore, a porosity function $f_{\text{pl}}(\varphi)$ is introduced that accounts for changes in grain contact area (hence contact stress magnitude) and transport path length (if a mass transfer process is involved), as porosity evolves (Spiers et al., 2004). The creep law describing creep deformation at grain contacts in a granular material can thus be rewritten as

$$\dot{\varepsilon}_{\text{pl}}\equiv E_{\text{pl}}(T,d,\sigma_n)f_{\text{pl}}(\varphi). \tag{11}$$

To satisfy the aforesaid criterion $f_{\text{pl}}(\varphi)$ needs to be chosen such that (1) it is dimensionless; (2) it yields a significant stress intensification as φ reaches φ_c, the critical state porosity for granular flow; and (3) at lower porosities it gives small values so that contact stress approaches the macroscopic stress as in typical rheological experiments. Following this approach, we assume

$$f_{\text{pl}}(\varphi) = (q - 2\varphi)^{-M}. \tag{12a}$$

Here M is the factor indicating the stress sensitivity to changes in porosity, and q is a geometrical constant, the value of which is 2 times the critical state porosity ($q = 2\varphi_c$). Previous experimental and theoretical

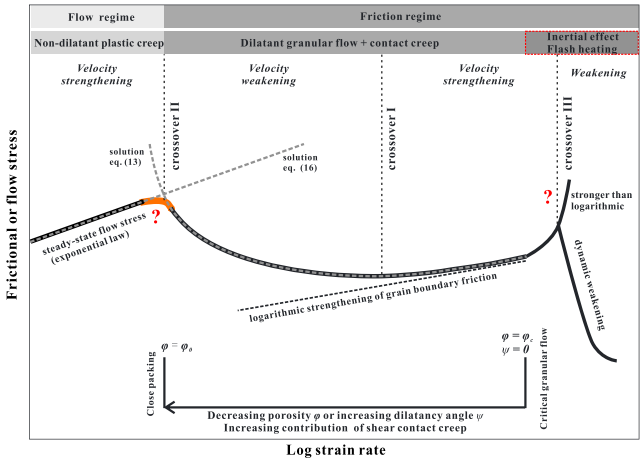

Figure 3. The schematic model of the steady state frictional or flow stress as a function of logarithmic strain rate for a granular fault gouge. (1) At low velocities, the model predicts velocity-strengthening behavior with deformation accommodated by non-dilatant plastic creep. In this flow regime, the granular material is densely compacted with a low porosity ($\varphi \approx \varphi_0$). (2) At intermediate velocities (the main concern of this paper), the imposed shear displacement is attributed to granular flow plus a thermally-activated creep mechanism. As the velocity increases, the friction behavior will be first controlled by dilatant granular flow that is mediated by compactional contact creep, giving rise to a velocity-weakening behavior and higher steady-state porosity; as the velocity increases further with the gouge approaching a critical state for granular flow, the frictional behavior will be controlled by grain boundary sliding which is inherently logarithmic strain rate-strengthening. At the critical state, the porosity reaches a critical value ($\varphi = \varphi_c$) and the average dilatancy angle becomes zero ($\psi = 0$). (3) At high velocities, friction may decrease substantially due to thermal weakening effects such as flash heating. Yet as proposed by recent studies (e.g., Kuwano et al., 2013), athermal dissipation processes like inertia could also become dominant at relatively high velocities, leading to stronger-than-logarithmic strain rate strengthening behavior (not discussed in the paper).

studies show that a function of this form works well for the geometry of a regular grain pack of a single constitutive component (e.g., quartz, calcite, halite, gypsum, or anhydrite), for porosities in the range of 5–40% (Niemeijer et al., 2002; Pluymakers & Spiers, 2014; Spiers et al., 2004). Take intergranular pressure solution (IPS), for example. M depends on the key process that controls a mass transfer process (i.e., dissolution, diffusion, and precipitation). Its value is 2 for a diffusion-controlled IPS process, 1 for dissolution controlled, and ~1 for precipitation controlled (Spiers et al., 2004).

For a simple cubic or body-centered cubic pack of initially spherical grains (Niemeijer & Spiers, 2007; Niemeijer et al., 2002; Renard et al., 1999), dilatation angle and porosity can be plausibly linked by the empirical relation that

$$\tan\psi = H(q - 2\varphi)^N. \tag{12b}$$

Here H is a constant representing the geometric pattern of the grains. For a 2-D model, H falls in the range $1/\sqrt{3}$ to $1/\sqrt{3}$ (Niemeijer & Spiers, 2007). N is the factor introduced to indicate the sensitivity of average dilatation angle varying with porosity. An empirical value of 1 is obtained for IPS. Again, q is 2 times the φ_c value, which, when $\varphi = \varphi_c$, yields the critical case at which $\tan\psi$ equals zero.

Substituting relations (11), (12a), and (12b) into (8a)–(8d) and solving the equations yields a general solution

$$\begin{aligned}
\tan\psi_{ss} &= H\left[\frac{L_t\lambda}{HV_{imp}}E_{pl}(T,d,\sigma_n)\right]^{1/(M+N)} \\
\varphi_{ss} &= \frac{1}{2}\left[q - \left(\frac{\tan\psi_{ss}}{H}\right)^{1/N}\right] \\
\tilde{\mu}_{ss} &= \tilde{\mu}^* + a_{\tilde{\mu}}\ln\left(\frac{V_{imp}}{V^*}\right) \\
\tau_{ss} &= \frac{\tilde{\mu}_{ss} + \tan\psi_{ss}}{1 - \tilde{\mu}_{ss}\tan\psi_{ss}}\sigma_n
\end{aligned} \tag{13}$$

With a specific creep law, this solution gives the steady state shear stress (τ_{ss}) and state ($\tan\psi_{ss}$ and φ_{ss}) of a granular material at a given frictional velocity (V_{imp}). See definition of all the parameters in Table 2.

3.2. Low-Velocity Flow Regime (Without Intergranular Slip)

The above derivations assume negligible shear contact creep (Figure 2c). Following the steady state solution given above, as slip rate decreases the average dilatancy angle will increase and the porosity will decrease. As porosity approaches zero or a given limit level, dilatant granular flow (and thus grain boundary sliding) will be inhibited or at least contribute negligibly to the strength (Figure 3). Accordingly, equations (5c) and (5d) can be omitted, and sample shear deformation is accommodated by the shear creep at grain contacts, rendering the fault system effectively into a flow regime (den Hartog & Spiers, 2014). The set of equations (5a)–(5d) will thus reduce to

$$V_{imp} = L_t\left[\lambda\gamma_{pl}^{sb} + (1-\lambda)\gamma_{pl}^{bulk}\right], \tag{14a}$$

$$-\frac{\dot{\varphi}}{1-\varphi} = \dot{\varepsilon}_{pl}. \tag{14b}$$

Equations (14a) and (14b) indicate that fault gouges in the flow regime will shear and compact contemporarily. In this case, a steady state cannot be achieved until the gouge has compacted to zero porosity or a

minimum porosity φ_0 (for instance, corresponding to the smallest possible free volume known as random close packing state (Scott & Kilgour, 1969)). The cutoff or terminal porosities has also been observed in many compaction experiments (e.g., Niemeijer et al., 2002; Spiers et al., 2004). Once achieved, porosity change is impossible ($\dot{\varphi} = 0$), the gouge will have the maximum, steady state flow strength.

As implied by equation (14a), deformation in the flow regime involves creep that occurs in both the shear band and bulk zones. Note here that the process of shearing of asperity junctions and the process of asperity creep at grain contacts may be governed by common or different mechanisms. We assume that the same creep law applies anisotropically in both the shear and normal directions. With a power creep law, deformation in the shear band and the bulk zone can be respectively expressed as

$$\dot{\gamma}_{\mathrm{pl}}^{\mathrm{sb}} = B_{\mathrm{pl}} \exp\left(-\frac{E_a}{RT}\right) \frac{\tau^n}{\left(d^{\mathrm{sb}}\right)^m} f_{\mathrm{pl}}(\varphi_0), \tag{15a}$$

$$\dot{\gamma}_{\mathrm{pl}}^{\mathrm{bulk}} = B_{\mathrm{pl}} \exp\left(-\frac{E_a}{RT}\right) \frac{\tau^n}{\left(d^{\mathrm{bulk}}\right)^m} f_{\mathrm{pl}}(\varphi_0). \tag{15b}$$

Here a preexponential factor B_{pl} is adopted for the shear component of contact creep (distinguished from A_{pl} for compaction, cf. equations (10a) and (10b)). Combining (14a), (15a), and (15b) gives the steady state flow stress

$$\tau_{\mathrm{ss}} = \left[\frac{1}{\Pi} \frac{V_{\mathrm{imp}}\left(d^{\mathrm{sb}}\right)^m}{B_{\mathrm{pl}} L_t f_{\mathrm{pl}}(\varphi_0)} \exp\left(\frac{E_a}{RT}\right)\right]^{1/n}, \tag{16a}$$

where $\Pi = \lambda + (1-\lambda)(d^{\mathrm{sb}}/d^{\mathrm{bulk}})^m$ is a dimensionless factor that unifies the deformation in both zones.

Similarly, for an exponential creep law, the steady state flow stress can be determined as

$$\tau_{\mathrm{ss}} = \frac{RT}{\Omega} \ln\left[\frac{1}{\Pi} \frac{V_{\mathrm{imp}}\left(d^{\mathrm{sb}}\right)^m}{B_{\mathrm{pl}} L_t f_{\mathrm{pl}}(\varphi_0)}\right] + \frac{E_a}{\Omega}. \tag{16b}$$

Both equations (16a) and (16b) indicate a rate-strengthening behavior in the flow regime.

3.3. Overall Profile of Shear Strength Versus Shear Strain Rate

Above we presented two end-member cases of the microphysical model, with the steady state solutions being given in (13) and (16a) and (16b), respectively. By checking the expressions without inputting any numbers, the model would predict an envelope of steady state frictional/flow stress as a function of shear strain rate as shown in Figure 3. The resultant curve indicates three different regimes of deformation:

1. *Low-velocity flow regime*. At low shear strain rates, the deformation is fully accommodated by dilationless plastic flow, exhibiting velocity-strengthening behavior. Compaction can occur in this regime but does not directly contribute to shear strength. The steady state flow strength is only achieved when the gouge compacts to a near-zero, threshold porosity (φ_0) (Figure 3). Away from near-zero porosity ($\varphi > \varphi_0$), the local stresses at grain contacts, as reflected by the porosity function (equation (12a)), will be higher, leading to a transient shear stress that is lower than the steady state (from equation (16a) or (16b) but with φ instead of φ_0). As compaction proceeds, the shear stress will increase and asymptotically approach the steady state as porosity reduces to φ_0.
2. *Intermediate-velocity frictional regime*. At intermediate strain rates, the slip is mainly attributed to dilatant granular flow (slip), which, when a steady state is achieved, is balanced by the compaction due to creep at grain contacts. On the one hand, dilatant granular flow is itself strain rate weakening with a sensitivity that decreases with increasing strain rate: the higher the slip rate, the more dilatant and less resistant the gouge tends to be (Niemeijer & Spiers, 2007). On the other hand, granular flow will produce sliding of the boundaries of grain neighbors over each other, which is inherently strain rate strengthening (Chen & Spiers, 2016; Nakatani, 2001; Rice et al., 2001) (see the dashed line in Figure 3). The competition between the two would cause a transition from velocity weakening to velocity strengthening as strain rate increases in this regime.
3. *High-velocity frictional regime*. At high shear strain rates, friction coefficient would decrease sharply due to a thermal weakening effect. Yet as proposed by recent studies, athermal energy dissipation processes can

also be important at relatively high slip rates, potentially leading to stronger-than-logarithmic velocity-strengthening behavior (Bar-Sinai et al., 2014).

Figure 3 presents an overall picture of the rate-dependent steady state shear strength of an arbitrary granular gouge material. Generally, the frictional/flow strength would pass through three transitions in its rate dependence as shear strain rate increases (Figure 3): from (1) rate strengthening (due to nondilatant plastic creep) at low slip rates, via (2) rate weakening and then back to strengthening at intermediate slip rates (due to the competition between dilatant granular flow and thermally activated asperity creep), and (3) finally to dynamic slip weakening (due to frictional heating). It is important to note that some transitions in the picture might be absent for some material. In the rest of this paper, we only focus on the intermediate-velocity regime in which the curve is characterized by a transition from rate weakening to strengthening (*Crossover I*).

4. Velocity Stepping and Expressions for RSF Parameters

In this section, we investigate the transient response of the CNS model to a stepwise change of load point velocity, wherein we derive the analytical expressions for the constitutive parameters a, b, and D_c. As in the framework of classical RSF laws (equations (4a)–(4c)), these parameters are defined in the vicinity of steady states. Here we first analyze the responses of the model (i.e., the direct and evolution effects) to a step of a finite magnitude from V^0 to V^1, and then seek their limits by assuming $V^1 \approx V^0$, which gives the expressions for a and b. As given in equation (4c), D_c is a slip distance that characterizes the poststep evolution of state, which usually follows an exponential function with displacement or elapsed time (Dieterich, 1979; Rice et al., 2001; Rice & Ruina, 1983). After a poststep velocity V^1 is achieved, friction is fully controlled by state such that the friction and state evolution curves share the same critical length scale (Rice & Ruina, 1983). Despite the fact that the responses of the Slowness and Slip laws differ far from steady state, in the vicinity of steady state, $\ln(V\theta/D_c) \approx V\theta/D_c - 1$ and the two laws are asymptotically identical (Ampuero & Rubin, 2008). In contrast, there is not an explicit length scale in the CNS model (cf. equations (2), (3), and (5a)–(5d)), but essentially, there should be one because it takes displacement for a shearing gouge to reach a new steady state. In addition, for the CNS model, there is arbitrariness in the choice of state variable to identify D_c. Here we choose porosity because it is a microphysically observable property and because the changes of porosity along with step changes in sliding velocity have also been shown to evolve over the same slip distance as friction, in both laboratory experiments and micromechanical models (e.g., Marone, Raleigh, & Scholz, 1990; Niemeijer & Spiers, 2006; Sleep, 1995; Sleep et al., 2000). We assume that porosity evolves exponentially with time (equation (29)), from which the expression of D_c can be identified.

Based on the above considerations, the equations for identifying RSF parameters in the framework of the CNS model, resembling equations (4a)–(4c), are as follows:

$$a = \frac{\partial \mu}{\partial(\ln V)}\Big|_{(V=V_{ss}^0,\varphi=\varphi_{ss}^0)} = \lim_{\Delta\to 0}(a_{eq}) = \lim_{\Delta\to 0}\left[\frac{\mu_{pk}-\mu_{ss}^0}{\ln(V^1)-\ln(V^0)}\right], \tag{17a}$$

$$b = \frac{\partial \mu}{\partial(\ln V)}\Big|_{(V=V_{ss}^1,\varphi=\varphi_{ss}^1)} = \lim_{\Delta\to 0}(b_{eq}) = \lim_{\Delta\to 0}\left[\frac{\mu_{pk}-\mu_{ss}^1}{\ln(V^1)-\ln(V^0)}\right], \tag{17b}$$

$$(a-b) = \frac{\partial \mu_{ss}}{\partial(\ln V)}|_{V=V_{ss}} = \lim_{\Delta\to 0}(a-b)_{eq} = \lim_{\Delta\to 0}\left[\frac{\mu_{ss}^1-\mu_{ss}^0}{\ln(V^1)-\ln(V^0)}\right], \tag{17c}$$

$$D_c = -\frac{V\partial\varphi}{\partial(d\varphi/dt)}\Big|_{(V=V_{ss}^1,\varphi=\varphi_{ss}^1)} = \lim_{\Delta\to 0}(d_0) = \lim_{\Delta\to 0}\left[\frac{V^1(\varphi_{ss}^1-\varphi_{ss}^0)}{\dot{\varphi}_{pk+}}\right]. \tag{17d}$$

In these equations, to be distinguished from the definitions of a, b, and D_c, the corresponding parameters for finite (large) velocity steps are referred to as equivalent values (notated as subscript "eq"). For equivalent slip distance, we use d_0 following previous studies (e.g., Marone et al., 2009).

4.1. Direct Effect (a)

We investigate an upward velocity step of $V^0 \to V^1$, starting from a prestep stable sliding state at velocity V^0. In the frictional regime, the shear component of plastic deformation on grain contacts (the first term on the right side of equation (5a)) contributes negligibly to the imposed slip rate (Figure 3), which is later confirmed

by the numerical simulations addressed in section 5.1. In this case, from the steady state solution given in (13), the prestep sliding can be expressed as

$$V^0 = L_t\lambda\dot{\gamma}_{gr}^0 = \frac{L_t\lambda\dot{\varepsilon}_{pl}^0}{\tan\psi_{ss}^0}, \tag{18a}$$

$$\mu_{ss}^0 = \frac{\widetilde{\mu}_{ss}^0 + \tan\psi_{ss}^0}{1 - \widetilde{\mu}_{ss}^0\tan\psi_{ss}^0}. \tag{18b}$$

After switching to a new load point velocity, we obtain

$$V^1 - \dot{\tau}/K = L_t\lambda\dot{\gamma}_{gr}, \tag{18c}$$

We assume a sufficiently stiff (fault) system without inertia, in which the imposed displacement rate can be changed instantaneously. As such, shear stress will have an instantaneous jump, accompanied by negligible slip before reaching the peak strength, and the state of the gouge will not change much ($\psi_{pk} \approx \psi_{ss}^0$). (The analytical solutions for the evolution of shear stress and state across the direct effect are given in the supporting information (SI), from which we propose a method to evaluate the average dilatancy angle.) The peak frictional strength is calculated as

$$\mu_{pk} = \frac{\widetilde{\mu}_{pk} + \tan\psi_{pk}}{1 - \widetilde{\mu}_{pk}\tan\psi_{pk}} = \frac{\widetilde{\mu}_{pk} + \tan\psi_{ss}^0}{1 - \widetilde{\mu}_{pk}\tan\psi_{ss}^0}. \tag{19}$$

The instantaneous change in friction coefficient can thus be determined as

$$\mu_{pk} - \mu_{ss}^0 = \frac{\left(\widetilde{\mu}_{pk} - \widetilde{\mu}_{ss}^0\right)\left(1 + \tan^2\psi_{ss}^0\right)}{\left(1 - \widetilde{\mu}_{pk}\tan\psi_{ss}^0\right)\left(1 - \widetilde{\mu}_{ss}\tan\psi_{ss}^0\right)}. \tag{20}$$

Right at the peak, the time derivative of shear stress is zero ($\dot{\tau} = 0$). From equation (18c), the intergranular slip rate at the peak is equal to

$$\dot{\gamma}_{gr}^{pk} = V^1/(L_t\lambda). \tag{21}$$

Without loss of generality, we assume prestep stable sliding as the reference. As such, we have $\dot{\gamma}_{gr}^0 = \dot{\gamma}_{gr}^*$ and $\widetilde{\mu}_{ss}^0 = \widetilde{\mu}^*$. The grain boundary friction coefficient at the peak point can be expressed as

$$\widetilde{\mu}_{pk} = \widetilde{\mu}^* + a_{\widetilde{\mu}}\ln\left(\dot{\gamma}_{gr}^{pk}/\dot{\gamma}_{gr}^*\right) = \widetilde{\mu}_{ss}^0 + a_{\widetilde{\mu}}\ln\left(V^1/V^0\right). \tag{22}$$

From equation (17a), the equivalent a value for a finite velocity step from V^0 to V^1 is calculated as

$$a_{eq} = \frac{\mu_{pk} - \mu_{ss}^0}{\ln\left(V^1/V^0\right)} = a_{\widetilde{\mu}}\frac{\left(1 + \tan^2\psi_{ss}^0\right)}{\left(1 - \widetilde{\mu}_{pk}\tan\psi_{ss}^0\right)\left(1 - \widetilde{\mu}_{ss}^0\tan\psi_{ss}^0\right)}. \tag{23a}$$

Considering an infinitesimally small perturbation in slip rate (i.e., $V^1/V^0 = 1 + \Delta$, where $\Delta \to 0$), the limit of (23a) can be obtained as

$$a = \lim_{\Delta\to 0}\left(a_{eq}\right) = a_{\widetilde{\mu}}\frac{\left(1 + \tan^2\psi_{ss}\right)}{\left(1 - \widetilde{\mu}_{ss}\tan\psi_{ss}\right)^2}. \tag{23b}$$

In deriving this expression we use $\widetilde{\mu}_{ss} = \widetilde{\mu}_{ss}^0$ and $\psi_{ss} = \psi_{ss}^0$, as the direct effect is determined from the prestep steady state (equation (17a)).

4.2. Evolution Effect (b)

Based on equation (8b), the steady state friction coefficient at V^1 is expressed as

$$\mu_{ss}^1 = \frac{\widetilde{\mu}_{ss}^1 + \tan\psi_{ss}^1}{1 - \widetilde{\mu}_{ss}^1\tan\psi_{ss}^1}, \tag{24}$$

where ψ_{ss}^1 is the average dilatancy angle at the new steady state. From (19) and (24), the difference between the peak and the new steady state friction coefficients can be formulated as

$$\mu_{pk} - \mu_{ss}^1 = -\frac{\left(1 + \widetilde{\mu}_{pk}\widetilde{\mu}_{ss}^1\right)\left(\tan\psi_{ss}^1 - \tan\psi_{ss}^0\right)}{\left(1 - \widetilde{\mu}_{pk}\tan\psi_{ss}^0\right)\left(1 - \widetilde{\mu}_{ss}^1\tan\psi_{ss}^1\right)}. \tag{25}$$

The grain boundary friction coefficient at V^1 can be expressed as

$$\widetilde{\mu}_{ss}^1 = \widetilde{\mu}^* + a_{\widetilde{\mu}}\ln\left(\frac{\dot{\gamma}_{gr}^1}{\dot{\gamma}_{gr}^*}\right). \tag{26}$$

At both the peak and the new steady state, the time derivatives of shear stress are zero ($\dot{\tau} = 0$). From equation (18c), the grain boundary friction coefficients should be the same, that is, $\widetilde{\mu}_{pk} = \widetilde{\mu}_{ss}^1$ (cf. equations (22) and (26)). Considering a small perturbation in slip rate, we have $\left(1 - \widetilde{\mu}_{pk}\tan\psi_{ss}^0\right) \approx \left(1 - \widetilde{\mu}_{ss}^1\tan\psi_{ss}^1\right)$. Equation (25) can thus be rewritten as

$$\mu_{pk} - \mu_{ss}^1 = -\frac{\left[1 + \left(\widetilde{\mu}_{ss}^1\right)^2\right]}{\left(1 - \widetilde{\mu}_{ss}^1\tan\psi_{ss}^1\right)^2}\left(\tan\psi_{ss}^1 - \tan\psi_{ss}^0\right). \tag{27a}$$

From the steady state solution (equations (8a)–(8d)), we have $\tan\psi_{ss} \propto V_{imp}^{-1/(M+N)}$. This makes (27a)

$$\mu_{pk} - \mu_{ss}^1 \approx -\frac{\left[1 + \left(\widetilde{\mu}_{ss}^1\right)^2\right]\tan\psi_{ss}^1}{\left(1 - \widetilde{\mu}_{ss}^1\tan\psi_{ss}^1\right)^2}\left[1 - \left(\frac{V^1}{V^0}\right)^{\frac{1}{(M+N)}}\right]. \tag{27b}$$

Following equation (17b), the equivalent b value for a finite velocity step can be calculated as

$$b_{eq} = \frac{\mu_{pk} - \mu_{ss}^1}{\ln\left(V^1/V^0\right)} = -\frac{\left[1 + \left(\widetilde{\mu}_{ss}^1\right)^2\right]\tan\psi_{ss}^1}{\left(1 - \widetilde{\mu}_{ss}^1\tan\psi_{ss}^1\right)^2}\frac{\left[1 - \left(V^1/V^0\right)^{1/(M+N)}\right]}{\ln\left(V^1/V^0\right)}. \tag{28a}$$

Supposing a small V step ($V^1/V^0 = 1 + \Delta$ where $\Delta \to 0$), using the Taylor expansion that $\ln(1 + \Delta) \approx \Delta + \ldots$, and $(1 + \Delta)^x = 1 + x\Delta + \ldots$, the limit of (28a) is

$$b = \lim_{\Delta\to 0}\left(b_{eq}\right) = \frac{\tan\psi_{ss}}{(M + N)}\frac{\left(1 + \widetilde{\mu}_{ss}{}^2\right)}{\left(1 - \widetilde{\mu}_{ss}\tan\psi_{ss}\right)^2}. \tag{28b}$$

In obtaining this expression, we use the relation $\widetilde{\mu}_{ss} = \widetilde{\mu}_{ss}^1$ and $\psi_{ss} = \psi_{ss}^1$. The rationale for doing this is that the evolution effect is evaluated with respect to the new steady state (equation (17b)).

Actually, the term $\frac{\tan\psi_{ss}}{(M+N)}$ expresses the logarithmic rate dependence of $\tan\psi_{ss}$. Resembling the definition of $a_{\widetilde{\mu}}$, we define $b_\psi \equiv -\frac{\partial(\tan\psi_{ss})}{\partial(\ln V)}$. Equation (28b) is thus rewritten as

$$b = b_\psi\frac{\left(1 + \widetilde{\mu}_{ss}{}^2\right)}{\left(1 - \widetilde{\mu}_{ss}\tan\psi_{ss}\right)^2}. \tag{28c}$$

4.3. Critical Slip Distance (D_c)

After an instant response, both friction and state of the gouge will evolve to a new steady state over a characteristic displacement, which is defined as the critical slip distance, D_c. Following the definition (equation (17d)), we will derive D_c from the evolution of one of the state variables of the CNS model, porosity. An exponential equation is employed to represent the porosity evolution; that is,

$$\varphi(t) = \varphi_{ss}^1 - \left(\varphi_{ss}^1 - \varphi_{ss}^0\right)\exp\left(-\frac{V^1 t}{D_c}\right), \tag{29}$$

where φ_{ss}^0 and φ_{ss}^1 are the porosities corresponding to prestep and new steady states, respectively, and t is the time elapsed since the peak friction. This exponential form necessarily results in the evolution of porosity in

our model consistent with that embodied in the state equations of the classical RSF laws (equations (2) and (3)), where D_c is originally defined (e.g., Dieterich, 1979). The time derivative of (29) gives

$$\dot{\varphi}(t) = \frac{V^1}{D_c}\left(\varphi_{ss}^1 - \varphi_{ss}^0\right)\exp\left(-\frac{V^1 t}{D_c}\right). \tag{30}$$

Right after the peak point (t = 0), equation (30) is determined as $\dot{\varphi}_{pk+} = V^1\left(\varphi_{ss}^1 - \varphi_{ss}^0\right)/D_c$. From equation (17d), the equivalent slip distance for the evolution of porosity in response to a finite (large) velocity step can be calculated as $d_0 = \dfrac{V^1\left(\varphi_{ss}^1 - \varphi_{ss}^0\right)}{\dot{\varphi}_{pk+}}$. Subsequently, D_c can be identified as

$$D_c = \lim_{\Delta\to 0}(d_0) = \lim_{\Delta\to 0}\left[\frac{V^1\left(\varphi_{ss}^1 - \varphi_{ss}^0\right)}{\dot{\varphi}_{pk+}}\right]. \tag{31}$$

To obtain D_c, one needs to know the two steady state porosities ($\varphi_{ss}{}^0$ and $\varphi_{ss}{}^1$) and the rate of change of porosity after the peak point ($\dot{\varphi}_{pk+}$), which can be determined as follows.

Right at the peak, the time derivative of shear stress is zero ($\dot{\tau} = 0$). From (5b), the compaction rate at V^1 can be expressed relative to the prestep steady state:

$$\frac{\dot{\varphi}}{1-\varphi} = \left(\frac{V^1}{V^0} - 1\right)\dot{\varepsilon}_{pl}. \tag{32}$$

Following a general creep law $\dot{\varepsilon}_{pl} \equiv E_{pl}\cdot f_{pl}(\varphi)$, we have $\dot{\varepsilon}_{pl} = \dot{\varepsilon}_{pl}^0 \dfrac{f_{pl}(\varphi)}{f_{pl}\left(\varphi_{ss}^0\right)}$. Equation (32) is expanded as

$$\frac{\dot{\varphi}}{1-\varphi} = \left(\frac{V^1}{V^0} - 1\right)\frac{\dot{\varepsilon}_{pl}^0}{f_{pl}\left(\varphi_{ss}^0\right)}(q - 2\varphi)^{-M}. \tag{33}$$

Integrating this equation over time yields

$$(q - 2\varphi) = \left[-2(M+1)(1-\varphi_{ss})\left(\frac{V^1}{V^0} - 1\right)\frac{\dot{\varepsilon}_{pl}^0}{f_{pl}\left(\varphi_{ss}^0\right)}t + \text{const}\right]^{\frac{1}{(M+1)}}. \tag{34}$$

This is the solution for postpeak porosity evolution. Note that in doing the integration, $(1-\varphi)$ is taken to be constant as $(1-\varphi_{ss})$, because its value changes only minimally during a small V step. In this expression, const is a constant that can be identified from the initial condition, giving const $= \left(q - 2\varphi_{ss}^0\right)^{(M+1)}$. By using the steady state solution, equation (34) can be reformulated as

$$(q - 2\varphi) = \left(q - 2\varphi_{ss}^0\right)\left(1 - \frac{t}{\varsigma}\right)^{1/(M+1)}, \tag{35}$$

where $\varsigma = \frac{L_t\lambda}{2(M+1)H(1-\varphi_{ss})\left(V^1 - V^0\right)}$. The time derivative of (35) is $\dot{\varphi} = \dfrac{\left(q - 2\varphi_{ss}^0\right)}{2(M+1)\varsigma}\left(1 - \dfrac{t}{\varsigma}\right)^{-\frac{M}{(M+1)}}$. By taking $t = 0$, the rate of porosity change right after the peak can be obtained

$$\dot{\varphi}_{pk+} = \frac{\left(q - 2\varphi_{ss}^0\right)}{2(M+1)\varsigma}. \tag{36}$$

Again, from the steady state solution, porosities at the two steady states are related to one another:

$$\left(q - 2\varphi_{ss}^1\right) = \left(q - 2\varphi_{ss}^0\right)\left(\frac{V^0}{V^1}\right)^{\frac{1}{N(M+N)}}. \tag{37}$$

Combining equations (36) and (37) with (31) yields the equivalent slip distance

$$d_0 = \frac{L_t\lambda}{2H(1-\varphi_{ss})}\frac{\left[1 - \left(V^0/V^1\right)^{\frac{1}{N(M+N)}}\right]}{\left(1 - V^0/V^1\right)}. \tag{38a}$$

Table 1
Microphysical Interpretation of Rate and State Frictional Parameters

Parameters	Microphysically derived expressions	Reference
	General expression for friction of a granular fault gouge	
μ	$\frac{\tilde{\mu}+\hat{\mu}}{1-\tilde{\mu}\hat{\mu}}$	Equations (5a)–(5d)
	Steady state solution	
$\tilde{\mu}_{ss}$	$\tilde{\mu}^{*}+a_{\tilde{\mu}}\ln\left(\frac{V_{imp}}{V^{*}}\right)$	Equation (13)
$\hat{\mu}_{ss}$	$H\left[\frac{L_t\lambda}{HV_{imp}}E_{pl}(T,d,\sigma_n)\right]^{\frac{1}{(M+N)}}$ or $\left(\frac{L_t\lambda H^2}{V_{imp}}\frac{A_d DCS}{RT}\frac{\sigma_n\Omega}{d^3}\right)^{1/3}$ for pressure solution	Equation (13)
φ_{ss}	$\varphi_{ss}=\frac{1}{2}\left[q-\left(\frac{\hat{\mu}_{ss}}{H}\right)^{1/N}\right]$	Equation (13)
μ_{ss}	$\frac{\tilde{\mu}_{ss}+\hat{\mu}_{ss}}{1-\tilde{\mu}_{ss}\hat{\mu}_{ss}}$	Equation (13)
	Parameters for describing transient behavior	
a	$a_{\tilde{\mu}}\frac{(1+\hat{\mu}_{ss}{}^2)}{(1-\tilde{\mu}_{ss}\hat{\mu}_{ss})^2}$	Equations (23a) and (23b)
b	$b_{\psi}\frac{(1+\tilde{\mu}_{ss}{}^2)}{(1-\tilde{\mu}_{ss}\hat{\mu}_{ss})^2}$	Equations (28a)–(28c)
D_c	$\frac{L_t\lambda}{2HN(M+N)(1-\varphi_{ss})}$	Equations (38a) and (38b)

Note. $\tilde{\mu}$ is grain boundary friction, and $\hat{\mu}\equiv\tan\psi$, is defined as dilatant friction coefficient. Further, we have $a_{\tilde{\mu}}=\frac{\partial\tilde{\mu}}{\partial(\ln V)}=\frac{kT}{\sigma_l\Omega}$ and $b_{\psi}=\frac{\partial\hat{\mu}}{\partial(\ln V)}=\frac{\hat{\mu}_{ss}}{M+N}$ specifying the logarithmic rate dependences of $\tilde{\mu}$ and $\hat{\mu}$, respectively. Refer to Table 2 for other parameters.

As given in supporting information Text S2, the same d_0 can be obtained from analyzing the postpeak evolution of shear stress. Therein, d_0 is defined as $d_0=\frac{\tau^{pk}-\tau^{1}_{ss}}{W^{*}}$ and W^{*} is the slip weakening rate $W^{*}=-\frac{d\tau}{dx}$ (Ampuero & Rubin, 2008).

When the velocity step size is small ($\Delta\mu_{dil}$ where $\tan\psi_{ss}$), the limit of d_0 is

$$D_c=\lim_{\Delta\to 0}(d_0)=\frac{L_t\lambda}{2HN(M+N)(1-\varphi_{ss})}. \tag{38b}$$

As also addressed in supporting information Text S2, the same critical length scale can be obtained by employing the average dilatancy angle to describe the state evolution.

4.4. Summary of the Expressions for RSF Parameters

Table 1 summarizes the microphysical interpretations of RSF parameters, a, b, and D_c. The friction rate dependence, $(a-b)$, can be determined as the difference between a and b; that is,

$$(a-b)=a_{\tilde{\mu}}\frac{(1+\tan^2\psi_{ss})}{(1-\tilde{\mu}_{ss}\tan\psi_{ss})^2}-b_{\psi}\frac{(1+\tilde{\mu}_{ss}{}^2)}{(1-\tilde{\mu}_{ss}\tan\psi_{ss})^2}. \tag{39}$$

The same result is obtained by determining the difference of two steady state shear stresses, following equation (17c) (see supporting information Text S3 for a detailed derivation).

Apparently, the values of a, b, and D_c do not directly depend on the creep mechanism at grain contacts, which will vary for different materials and conditions. In a sense, these expressions are general and can apply to any granular material, provided that intergranular flow and an arbitrary creep process at grain contacts are the dominant deformation mechanisms.

5. Numerical Implementation of the Microphysical Model Versus RSF Laws

In this section, we first apply the CNS model to simulate a laboratory fault filled with a carbonate gouge and subjected to hydrothermal conditions. Under these conditions, IPS is expected to be the dominant contact creep mechanism. The analytical expressions obtained above, for both the steady state and the transient response, are compared with the numerical results. Inserting the parameters obtained into classical RSF laws (Slowness and Slip laws), we next conduct forward modeling, comparing the results with the direct predictions of the numerically implemented CNS model.

5.1. Simulations With Microphysical Friction Model

The geometric model, microstructural parameters, and pressure-temperature conditions used here are the same as previously employed by Chen and Spiers (2016). They are summarized as follows: (1) a 50 μm thick shear band localized at the margin of a 0.8 mm thick gouge layer; (2) average grain sizes of 2 μm and 20 μm in the shear band and bulk gouge, respectively; and (3) imposition of constant or variable shear velocity at the load point to shear the sample which is subjected to 50 MPa effective normal stress and 80°C hydrothermal conditions. Under these conditions, granular flow and diffusion-controlled intergranular pressure solution (IPS) are inferred to be the dominant deformation mechanisms (Chen et al., 2015). As reported in compaction experiments on calcite (e.g., Zhang et al., 2010), the compaction strain rate by grain boundary diffusion controlled IPS can be expressed as a linear law as $\dot{\varepsilon}_{\mathrm{pl}} = A_d \frac{DCS}{d^3}\frac{\sigma_n \Omega}{RT} f_d(\varphi)$. In this equation, σ_n is the applied effective normal stress, T is the absolute temperature (K), and φ is the porosity. Furthermore, A_d is a geometric constant, D is the diffusivity of the solute within the grain boundary fluid (m^2/s), C is the solubility of the solid species in the solution (m^3/m^3), S is the effective thickness of the grain boundary fluid phase (m), Ω is the molar volume of the solid phase (m^3/mol), R is the universal gas constant (8.31 J mol^{-1} K^{-1}), and d is the average grain size of the shear band. For porosities falling in the range from 5% to 40%, the porosity function can be approximated as $f_{\mathrm{pl}}(\varphi) \approx (q - 2\varphi)^{-2}$ (Spiers et al., 2004). An empirical relation is used to link the dilatation angle and porosity such that $\tan\psi = H(q - 2\varphi)$ (Niemeijer & Spiers, 2007; Renard et al., 1999). For grain boundary friction, we use a reference friction coefficient of 0.60 at 1 μm/s, with a logarithmic rate dependence of 0.006 (Chen & Spiers, 2016).

To simulate the transient behavior, we represent a fault as a spring-slider system composed of a linear spring activated by the imposition of a constant velocity at a load point, assuming no inertia. The difference in velocity between the load point and slider generates the distortion of the spring; that is,

$$\dot{\tau}/K = V_{\mathrm{imp}} - V, \tag{40}$$

where V_{imp} is the slip rate at the load point (m/s), τ is the shear stress (Pa), K is the stiffness of the surroundings of the fault (Pa/m), and V is the sample slip velocity expressed via equation (5a). For computational convenience, the constitutive equations (5a)–(5d) together with (40) can be written into a pair of ordinary differential equations (ODEs), specifying the rate of change of shear stress (τ) and state (φ):

$$\frac{\dot{\tau}}{K} = V_{\mathrm{imp}} - L_t\left[\lambda\dot{\gamma}_{\mathrm{pl}}^{\mathrm{sb}} + (1-\lambda)\dot{\gamma}_{\mathrm{pl}}^{\mathrm{bulk}}\right] - L_t\lambda\dot{\gamma}_{\mathrm{gr}}^{*}\exp\left[\frac{\tau(1-\widetilde{\mu}^{*}\tan\psi) - \sigma_n(\widetilde{\mu}^{*} + \tan\psi)}{a_{\widetilde{\mu}}(\sigma_n + \tau\tan\psi)}\right], \tag{41a}$$

$$\frac{\dot{\varphi}}{(1-\varphi)} = \tan\psi\dot{\gamma}_{\mathrm{gr}}^{*}\exp\left[\frac{\tau(1-\widetilde{\mu}^{*}\tan\psi) - \sigma_n(\widetilde{\mu}^{*} + \tan\psi)}{a_{\widetilde{\mu}}(\sigma_n + \tau\tan\psi)}\right] - \dot{\varepsilon}_{\mathrm{pl}}. \tag{41b}$$

As in our previous study (Chen & Spiers, 2016), the ODEs are solved using the finite element package COMSOL. All the parameters used are based on the experimental results on a natural carbonate fault gouge or pure calcite (Chen et al., 2015; Verberne et al., 2013). See details in Chen and Spiers (2016) and Table 2 for the model settings.

We first simulate the stationary state by setting $\dot{\tau} = 0$ and $\dot{\varphi} = 0$ in the above set of equations. As shown in Figure 4, the steady state friction coefficients predicted for different velocities indicate a transition from velocity weakening to strengthening as slip rate increases, with the $(a - b)$ values also increasing from a negative value of −0.035 at 20 nm/s, via ~0 at ~5 μm/s, to +0.0055 at 1.0 mm/s. With the same parameters, this result is the same as Figure 5 given by Chen and Spiers (2016). Correspondingly, the steady state porosity exhibits an

Table 2
Explanation of Symbols Used in the Implementation of the Model

Symbol	Description (unit)	Value	Symbol	Description (unit)
σ_n	effective normal stress (Pa)	5×10^7	φ	porosity
T	absolute temperature (K)	353	φ_0	porosity at random close packing state
K_{ref}	a reference stiffness (Pa/m)	6×10^{10}	φ_c	critical state porosity for granular flow
V_{imp}	imposed slip rate at load point (μm/s)	1–5	a_c	average contact area (m^2)
L_t	thickness of the entire gouge layer (m)	8×10^{-4}	μ	macroscopic friction coefficient
λ	localization degree	0.0625	$\widetilde{\mu}$	grain boundary (gb) friction coefficient
φ_0^{bulk}	initial porosity of bulk gouge	0.32	$\hat{\mu}$	dilatant friction coefficient (=tanψ)
d^{sb}	average grain size of shear band (m)	2×10^{-6}	b_ψ	logarithmic rate dependence of tanψ
d^{bulk}	average grain size of the bulk gouge (m)	2×10^{-5}	$\dot{\varepsilon}$	compaction strain rate (s^{-1})
q^{sb}	2 × critical porosity for shear band	0.4	$\dot{\gamma}$	shear strain rate (s^{-1})
q^{bulk}	2 × critical porosity for bulk gouge	0.7	E_a	activity energy for a general creep law (J/mol)
H	geometrical parameter for grain shape	0.577	m	grain size sensitivity in a general creep law
A_d	rate constant for diffusion-controlled IPS	100	n	stress sensitivity in a general creep law
DS	diffusion coefficient × gb thickness (m^3/s)	2×10^{-20}	a	RSF parameter for a direct effect
C	solubility of the solute in fluid film (m^3/m^3)	3.95×10^{-6}	b	RSF parameter for an evolution effect
Ω	molar volume of solid phase (m^3/mol)	3.69×10^{-5}	θ	state variable in RSF laws (s)
$\widetilde{\mu}^*$	reference gb friction coefficient at 1 μm/s	0.6	D_c	characteristic slip distance in RSF laws (m)
$a_{\widetilde{\mu}}$	logarithmic rate dependence of gb friction	0.006	d_0	equivalent dynamic slip(-weakending) distance
M	sensitivity of stress intensification to porosity	2	W^*	dynamic slip-weakening rate (= − dμ/dx)
N	sensitivity of dilatation angle to porosity	1	t	time (s)
V	slip velocity on deforming sample (m/s)		t_{ins}	characteristic time in an instantaneous response (s)
K	stiffness of a simulated fault (Pa/m)		Δ	an infinitesimal perturbation
τ	shear stress (Pa)			
ψ	dilatation angle			
subscripts			superscripts	
pl	plastic creep on contacts		0, 1	prestep state, poststep state
gr	granular flow		sb	shear band
ss	steady state		bulk	bulk gouge
pk	peak point		*	a reference state
pk+	time just after the peak			
eq	equivalent quantities for large V steps			

increase from 13.0% to 19.5% as velocity changes in the same range. Notably, with increasing velocity, porosity approaches the critical-state value (φ_c = 20%).

The steady state can be analytically obtained from the general solution by letting $\dot{\varepsilon}_{pl} = A_d \frac{DCS}{d^3}\frac{\sigma_n \Omega}{RT}$ and using an M and N value of 2 and 1, respectively. As given in Table 1, the expressions are the same as those obtained by Niemeijer and Spiers (2007) (assuming no cohesion). The values of steady state friction coefficients and porosities calculated from these expressions are consistent with the numerical results over a wide range of sliding velocities (Figure 4). Visible discrepancy only appears when velocities fall below 10^{-8} m/s, where the shear plastic creep becomes increasingly important. Since the numerically implemented model includes the shear creep at grain contacts (the first term on the right side of equation (5a)) and our theoretical analysis does not, the fact that they are consistent confirms the prescribed assumption that the shear creep rate is negligibly small in the frictional regime at the simulated conditions.

Next, to validate the expressions obtained for a, b, and D_c (Table 1), we simulated a velocity-stepping test by abruptly changing the displacement rate by a small magnitude (1 → 1.1 μm/s). To get a clear separation between the direct effect and the evolution effect that allows for comparison with the analytical result, we used a high spring stiffness (100 times the apparatus stiffness employed by Chen et al., 2015). As shown in Figure 5a, the result of friction coefficient versus time shows an instantaneous jump followed by an exponential decay to a new steady state, which, compared with the prestep steady state, indicates velocity-weakening behavior. Accordingly, the porosity shows a monotonic increase by ~ 0.05% (Figure 5b), sharing the same evolution distance as friction coefficient.

We will now compare these results with the analytical results. Using the expressions for a, b, and D_c (Table 1), the direct effect, the evolution effect, and critical slip distance can be calculated as $a\ln(V^1/V^0)$, $b\ln(V^1/V^0)$, and

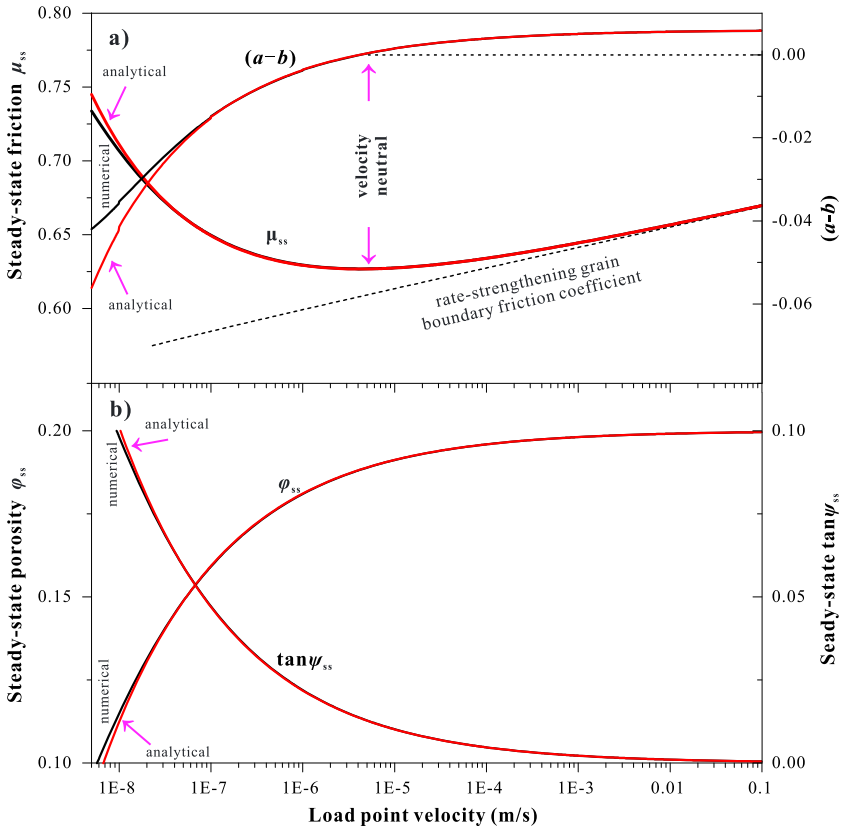

Figure 4. The prediction of (a) steady state friction coefficient μ_{ss} and $(a - b)$ and (b) steady state porosity φ_{ss}, and $\tan\psi_{ss}$, as a function of the logarithm of load point velocity from the CNS model (within the intermediate-velocity friction regime shown in Figure 3). As indicated respectively by the black and red lines, consistent results are obtained from the numerically implemented model and the analytical solutions derived. All the calculations are based on a simulated carbonate gouge sheared at hydrothermal conditions (see the text).

D_c, respectively. As shown in Figures 5a and 5b, all of these values agree satisfactorily with the numerical results. These results also show that the evolution curves of friction coefficient and porosity can be characterized by same critical length scale D_c (cf. Figures 5a and 5b), as is mathematically proven in supporting information Text S2. Finally, we note that here a 1.1-fold velocity step is used for the validation of the analytical expressions derived. As demonstrated in the following section, discrepancies will appear between the numerical and analytical results for large velocity steps.

5.2. Forward RSF Modeling and Comparison

We perform forward RSF modeling with the parameters calculated from our analytical expressions, which allows for a comparison between RSF and the microphysical CNS model. Both the Slowness (2) and Slip laws (3) are used as the state equations. The input values of a, b, and D_c used are calculated from (23a) and (23b), (28a)–(28c), and (38a) and (38b), respectively (Table 1). Except where otherwise stated, the fault stiffness is the same as that used in the previous numerical modeling (6×10^{12} Pa/m, previous section).

Again, we simulate a small velocity step from 1 μm/s to 1.1 μm/s. The initial friction coefficient (at $V^0 = 1$ μm/s) is set according to the steady state solution. The initial state θ is set to be D_c/V^0, which makes the fault initially at steady state ($d\theta/dt = 0$). This forward RSF modeling is performed using COMSOL. As shown in Figure 6a, the evolution of frictional strength predicted by the RSF laws (i.e., Slowness and Slip laws) agrees exactly with the prediction from the microphysical model, suggesting that the RSF laws and the CNS model are asymptotically identical in the vicinity of steady state. The microphysical model and the RSF laws use different state variables, namely, porosity φ and state θ (typically interpreted as average lifetime of contact asperities). Both state variables exhibit a monotonous change with shear displacement. To compare their evolution curves, they are normalized using the relation that $x_{nor} = |(x - x_0)/(x_{max} - x_{min})|$, where x represents φ or θ, so that x_{nor}

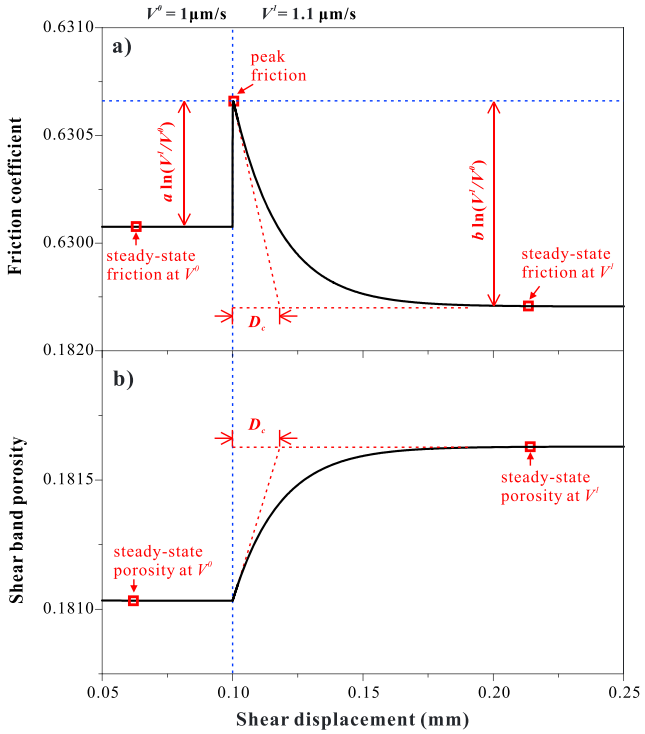

Figure 5. Numerical results of the microphysical model, showing the evolution of (a) friction coefficient and (b) shear band porosity in a small velocity-stepping test (1 → 1.1 μm/s). Analytical results of the steady state friction coefficients and porosities (μ_{ss}^0, μ_{ss}^1, φ_{ss}^0, and φ_{ss}^1), the peak friction coefficient (μ_{pk}), and the critical slip distance (D_c), as indicated by red squares or arrows, are added for comparison. The numerical and analytical results are in satisfactory agreement.

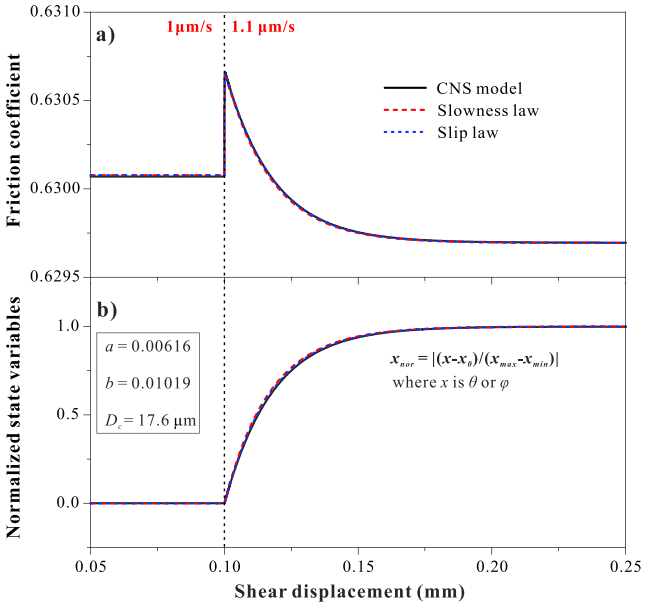

Figure 6. Comparison of the (a) CNS and (b) RSF modeling results of a small velocity-stepping test (1 → 1.1 μm/s). The RSF parameters used (i.e., a, b, and D_c) are calculated from the analytical expressions given in Table 1. The CNS model uses the same parameters as the model shown in Figure 5.

changes from 0 to 1. As shown in Figure 6b, the normalized state variables from all the three laws are fully consistent, evolving exponentially to a new steady state over the same critical slip distance. Notwithstanding being entirely irrelevant, comparing φ and θ as such is plausible since any ambiguous (nonlinear) relation can be linearized with respect to a small perturbation to steady state. This is further confirmed by our theoretical analysis (supporting information Text S2), which shows that the same critical slip distance can be derived from the poststep evolution of different state variables, although they are strongly nonlinearly related (e.g., φ and $\tan\psi$ are linked by a power law as equation (12b)). The above forward RSF modeling demonstrates the validity of the analytical expressions for the RSF parameters as derived in this study. It suggests that our microphysical model is somehow equivalent to the classical RSF laws, at least in the stable sliding regime.

When subjected to large perturbations, the RSF parameters are not constant anymore. To distinguish from the standard a, b, and D_c that are inherent for small perturbations, corresponding properties for large velocity steps are referred to as "equivalent values" (denoted with subscript eq, see the definition also in section 4). Figure 7 presents the equivalent a, b, $(a-b)$, and D_c values that vary with the size of the velocity steps (V^1/V^0), again taking a carbonate gouge as an example and using the same prestep velocity of 1 μm/s. By definition, the direct effect depends only on the prestep velocity (equation (23a)), which, for velocity steps investigated here, should be the same, yielding $a_{eq} = a$ (Figure 7a). The equivalent $(a-b)$ can be determined from the two consecutive steady state frictional strength: $(a-b)_{eq} = (\mu_{ss}^1 - \mu_{ss}^0)/\ln(V^1/V^0)$. The b_{eq} value is the difference between a and $(a-b)_{eq}$, which shows a decrease with increasing V^1/V^0 (Figure 7a). From the expression derived (equations (38a) and (38b)), D_c does not depend on either the size or the sign of a velocity step, and its variations shown in Figure 7b are due to a weak rate dependence of steady state porosity. Although D_c does not depend on V^1/V^0, the equivalent slip(-weakening) distance d_0 does, as will be discussed in the following.

It is the dynamic response of a fault that distinguishes one friction law from another. It is well known that different state equations can cause distinct frictional responses to large perturbations, leading to very different earthquake nucleation styles in numerical models (Ampuero & Rubin, 2008; Rubin & Ampuero, 2005). To gain some insight on this issue for the CNS model, we first investigate a velocity step from 1 to 5 μm/s and compare with the RSF modeling results. The RSF parameters are calculated from the expressions derived (see the inset of Figure 8). By using relatively lower spring stiffness (6×10^{11} Pa/m), the frictional curves predicted show nonlinear changes across the direct effect (Figure 8), which allows for the comparison with the analytical solution for the instantaneous response (supporting information Text S1). Coincidently, the postpeak friction curve of the CNS model falls between the predictions by the Slowness and the Slip laws (Figure 8). Note that it does not make much sense to compare the state evolution from different laws as in Figure 6b because any nonlinearity embodied in the state equations could be exaggerated in response to large perturbations.

Next, we compare the predictions from the CNS model and the RSF laws, for velocity upstep and downstep of up to 4 orders of

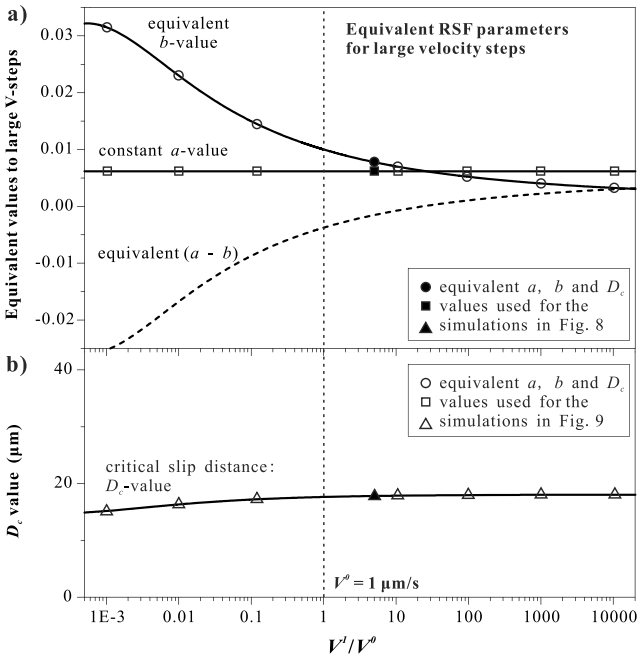

Figure 7. Equivalent RSF parameters for large perturbations (i.e., a, b_{eq}, $(a-b)_{eq}$, and D_c) as a function of velocity perturbation size. Here we drop the subscript eq for a_{eq} and $D_{c(eq)}$, because their values do not change with the velocity step size (the D_c value appears to change but this is due to the rate dependence of steady state porosity). All the results are calculated with a prestep velocity V^0 of 1 μm/s. The equivalent values of a, b, and D_c for velocity steps of magnitudes 5, $10^{\pm1}$, $10^{\pm2}$, $10^{\pm3}$, and 10^{+4}, as indicated by circles, squares, and triangles, are used in RSF simulations of Figures 8 and 9.

magnitude. In this exercise, we again use V^0 of 1 μm/s but vary V^1 from 1 nm/s to 10 mm/s. Figures 9a and 9b show the poststep evolution of friction coefficient predicted by the CNS model and the RSF laws, for velocity upstep and downstep, respectively. Note that to eliminate the effects of finite stiffness on the frictional response obtained using different constitutive laws, here we use infinite spring stiffness (Ampuero & Rubin, 2008). For the Slowness and Slip laws simulations, the equivalent RSF parameters are calculated from the analytical expressions given in section 4 (as also indicated in Figure 7). Since the equivalent b value (b_{eq}) is strongly velocity step size dependent, the intercepts at zero slip distance in Figure 9, which are essentially the apparent evolution effects ($\mu_{pk}-\mu_{ss}^{1}$), are unevenly spaced. In general, for all the velocity steps simulated, the evolution curve from the CNS model falls between the predictions by the Slowness and the Slip laws. The behavior of CNS model is closer to that of the Slowness law. The following observations of similarity can be made: (1) For velocity upsteps, the evolution curves of the CNS model and the Slowness law share more or less the same slip-weakening rate ($-d\mu/dx$) (Figure 9a). (2) For both laws, the critical length scale for the evolution of the frictional strength to approach steady state (d_0) increases with the size of the steps (Figure 9a). (3) For both laws, the frictional responses are asymmetric for velocity upstep and downstep and the d_0 values are larger than D_c for upsteps but smaller than D_c for the downsteps (cf. Figures 9a and 9b). The reason for this similarity can be found by variable substitutions, which allows us to reformulate the CNS model into an equivalent form of the Slowness law (see supporting information Text S4). In spite of this mathematical similarity, the CNS model does show a few peculiarities that distinguish it from the Slowness law, which, in a sense, are similar to the features possessed by the Slip law. For instance, the frictional responses to both velocity upstep and downstep predicted by the CNS model show a slip-weakening rate that decreases with cumulative slip. This nonlinearity is inferred to originate from the fact that the state evolution with displacement in the CNS model follows a power law, with a power exponent of less than 1 (equation (35)), while in the Slowness law it follows an exponential function (equation (2)). This interpretation is further confirmed if d_0 is expressed as a function of the sign of a velocity step (V^1/V^0), for different laws:

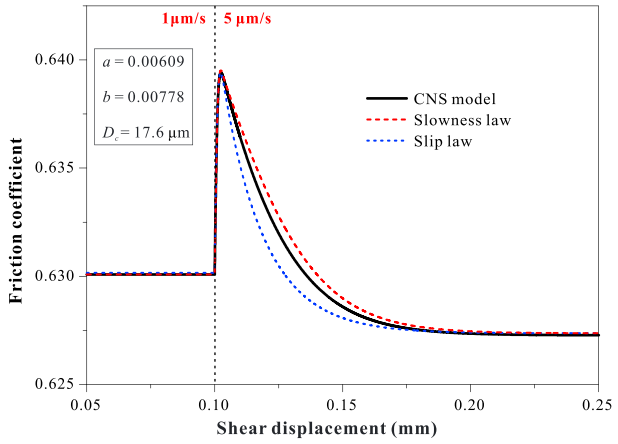

Figure 8. Comparison of CNS and RSF modeling of a velocity-stepping test from 1 to 5 μm/s. The spring stiffness is set 10 times smaller than that used in Figures 5 and 6. All others parameters are the same.

1. As given by equation (38a) or (B12), the d_0 value for the CNS model can be calculated as

$$d_0|_{CNS}=\frac{L_t\lambda}{2H(1-\varphi_{ss})}\frac{\left[1-\left(V^0/V^1\right)^{\frac{1}{N(M+N)}}\right]}{\left(1-V^0/V^1\right)}. \tag{42a}$$

2. For the Slip law, d_0 is independent of either the size or the sign of the step in velocity and should be equal to the critical slip distance; that is,

$$d_0\big|_{Slip}=D_c=\frac{L_t\lambda}{2HN(M+N)(1-\varphi_{ss})}. \tag{42b}$$

3. For the Slowness law, the postpeak evolution of frictional strength with slip is linear with a slope of $-b/D_c$ when the velocity upsteps push the fault far above steady state. In general, the slip-weakening rate for both upstep and downstep is expressed as

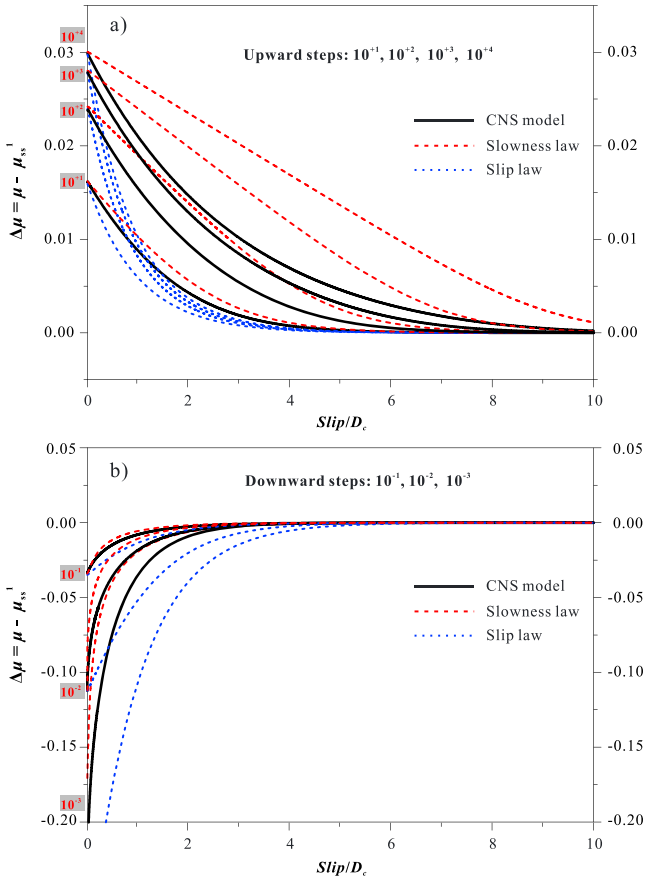

Figure 9. Friction behavior of the CNS model, the Slowness law, and the Slip law, in response to (a) velocity upsteps of magnitudes 10^1, 10^2, 10^3, and 10^4 and to (b) velocity downsteps of magnitudes 10^{-1}, 10^{-2}, and 10^{-3}. The prestep velocity V^0 is 1 μm/s for all the simulations. See detailed explanation in the text.

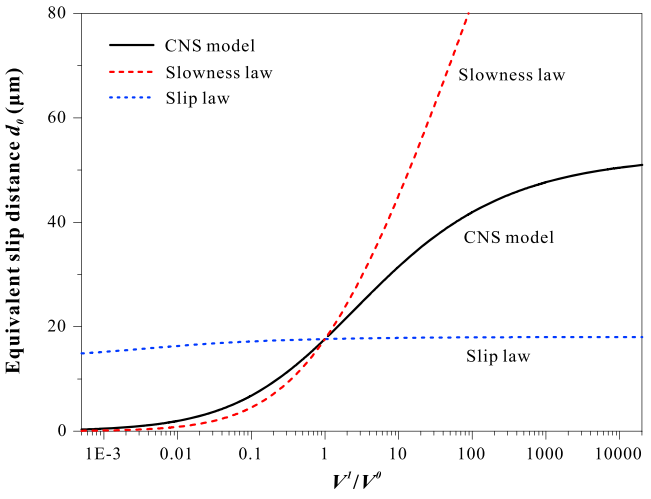

Figure 10. Comparison of equivalent slip(-weakening) distances of the CNS model, the Slip law, and the Slowness law, in response to large velocity steps of up to 4 orders of magnitude. The calculations are based on the analytical expressions (42a)–(42c), and with a prestep velocity of 1 μm/s. The results for different friction laws are consistent with the numerical results which show that the frictional curves of the CNS model always fall between the predictions by the Slowness and the Slip laws (cf. Figure 9).

$W^* = -\frac{d\mu}{dx} = \frac{b}{D_c} - \frac{b}{V^1\theta^0} = \frac{b}{D_c}\left(1 - \frac{V^0}{V^1}\right)$ (see equation (29) of Rubin & Ampuero, 2005). Correspondingly, the d_0 value can be determined as

$$d_0|_{\text{Slowness}} = \frac{b\ln(V^1/V^0)}{W^*} = D_c\frac{\ln(V^1/V^0)}{(1 - V^0/V^1)} = \frac{L_t\lambda}{2HN(M+N)(1-\varphi_{ss})}\frac{\ln(V^1/V^0)}{(1 - V^0/V^1)} \quad . \tag{42c}$$

With parameters from a simulated calcite slip zone, the calculated d_0 values are plotted as a function of V^1/V^0 for the three friction laws (Figure 10). Clearly, the d_0 values from the CNS model are between that from Slip and Slowness laws, for both velocity upstep and downstep, which can explain why the frictional response of CNS model always falls between the predictions by the Slowness and Slip laws (Figures 8 and 9). This result is also consistent with the complex observation from the numerical simulations that the d_0 values of the CNS model are larger than that of the Slowness law for upsteps, but smaller for downsteps (cf. Figures 9a and 9b).

Detailed comparison of the CNS model with RSF laws, related to earthquake nucleation and healing processes, includes investigating the characteristic fracture energy (Ampuero & Rubin, 2008), the critical nucleation size (Dieterich, 1992; Rubin & Ampuero, 2005), and the postseismic slip and restrengthening behavior (Beeler et al., 1994), as well as simulations of the nucleation styles with numerical models in combination with continuum elasticity (e.g., Bhattacharya & Rubin, 2014). However, these are all beyond the scope of the present paper.

6. Discussions

6.1. Frictional Strength of a Granular Fault Gouge

It is appealing that the different regimes of friction from slow to high slip rates can be described using a single physics-based friction law (cf. Baumberger et al., 1999; Estrin & Bréchet, 1996; Putelat et al., 2007). The present model assumes that the frictional strength of a granular fault gouge is controlled by plastic creep at grain contacts and intergranular flow (slip) process (Figure 2c). The model predicts a velocity-strengthening behavior in the low strain rate regime caused by nondilatant plastic flow, which, as shear strain rate increases, transitions to velocity-weakening and back to velocity-strengthening behavior, with the frictional strength being controlled by the steady state porosity and thus by the competition between shear-induced dilatation and time-dependent compaction by an arbitrary creep mechanism; in the high strain rate regime, dynamic slip (velocity-) weakening behavior due to mechanisms activated by frictional heating is expected (Figure 3). In the following, our discussion will focus on the intermediate-velocity regime. The transitional behavior in low and high strain rate regimes (*Crossovers II and III* in Figure 3) will be discussed in a future contribution.

In the frictional regime, the shear strength is determined by $\tau = \frac{\tilde{\mu} + \tan\psi}{1 - \tilde{\mu}\tan\psi}\sigma_n$. Referring to Coulomb's definition of internal sliding

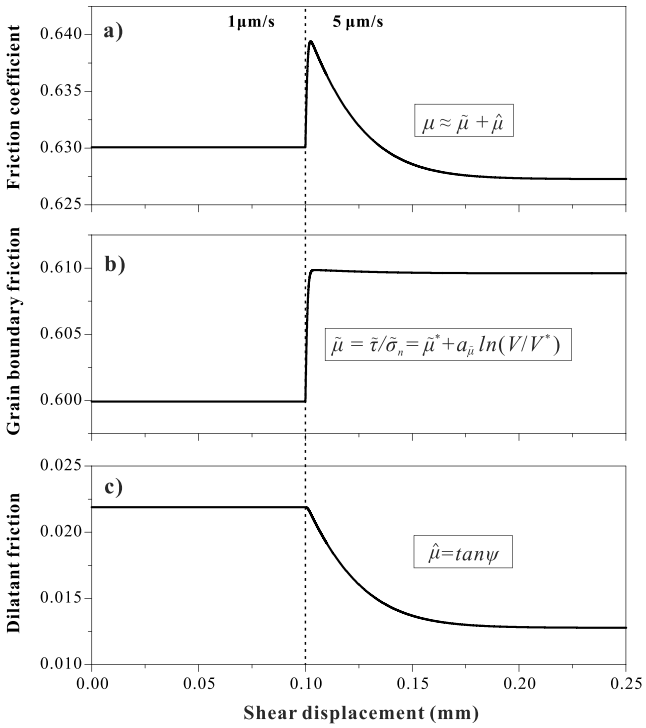

Figure 11. A velocity step example illustrating that (a) the macroscopic friction coefficient of a granular fault gouge consists of the two components, namely, (b) grain boundary friction, and (c) friction due to intergranular dilatation (or dilatant friction). The results are the same as in Figure 7 for a velocity step from 1 to 5 μm/s.

friction with respect to friction angle, we define $\hat{\mu} \equiv \tan\psi$ as the dilatant friction that is required for a shearing granular material to sustain the current dilatation state, as is microstructurally specified by the average dilatancy angle ψ (see the definition in Figure 2). As such, this equation becomes $\tau = \frac{\tilde{\mu} + \hat{\mu}}{1 - \tilde{\mu}\hat{\mu}}\sigma_n$. This relation indicates that the frictional strength of a granular fault gouge is attributed to two components, namely, grain boundary friction and friction due to intergranular dilatation. Since ψ is usually small in the intermediate frictional regime (notably less than 0.1 for calcite at the simulated conditions, Figure 4), the macroscopic friction of a granular fault gouge can be approximated to the first order as $\mu \approx \tilde{\mu} + \hat{\mu}$ (Figure 11).

At steady state, the microstructure, hence porosity and average dilatancy angle, characterizing the granular gouge must be constant. This means that the competing processes, namely, dilatation due to granular flow and compaction by creep mechanism at grain contacts, should balance each other. This balance decides the steady state porosity and thus the frictional strength. The role of a creep mechanism in determining the shear strength is simply one of determining the steady state porosity, that is, the porosity at which shear-induced dilatation is balanced by compaction through creep at stressed grain contacts.

In the present model, $\tilde{\mu}$, depending on the slip rate at grain contacts, increases with shear strain rate, while $\hat{\mu}$, as reflected by the steady state porosity (Figure 4), shows a strain rate-weakening behavior. For a transient frictional process, their combined effects decide the overall strain rate dependence of the material, as discussed in the following sections (6.2–6.4).

6.2. Microphysical Interpretation of RSF Parameters (a, b, and D_c, and ($a - b$))

6.2.1. Direct Effect (a Value)

The exponential dependence of shear velocity on shear stress, which appears as the direct effect in the context of RSF laws, is commonly explained by a physical model in which shear creep of asperity contacts obeys an exponential constitutive relation (Baumberger & Caroli, 2006; Beeler et al., 2007; Nakatani, 2001; Rice et al., 2001). This effect describes the instantaneous dependence of fault strength on deformation rate. Based on our microphysical framework, the direct effect is expressed as $a = a_{\tilde{\mu}}^{\sim}\frac{(1 + \hat{\mu}_{ss}{}^2)}{(1 - \tilde{\mu}_{ss}\hat{\mu}_{ss})^2}$, where $a_{\tilde{\mu}}^{\sim}$ is the logarithmic rate dependence of $\tilde{\mu}$, defined as $a_{\tilde{\mu}}^{\sim} \equiv \frac{\partial\tilde{\mu}}{\partial(\ln V)}$. Actually, the expression of the a value can be obtained by differentiating the friction law $\tau = \frac{\tilde{\mu} + \hat{\mu}}{1 - \tilde{\mu}\hat{\mu}}\sigma_n$. For an instantaneous response, the state (ψ) and thus the $\hat{\mu}$ value can be taken as constants so that we have

$$a = \frac{\partial\mu}{\partial(\ln V)}\Big|_{(\psi=\psi_{ss})} = \frac{\partial\mu}{\partial\tilde{\mu}}\frac{\partial\tilde{\mu}}{\partial(\ln V)} = a_{\tilde{\mu}}^{\sim}\frac{(1 + \hat{\mu}_{ss}^2)}{(1 - \tilde{\mu}_{ss}\hat{\mu}_{ss})^2}. \quad (43)$$

As derived from the lattice scale and based on the mechanical work on an elementary energy barrier for contact sliding (Chen & Spiers, 2016), $a_{\tilde{\mu}}^{\sim}$ is expressed as

$$a_{\tilde{\mu}}^{\sim} = \frac{kT}{\sigma_I\Omega}, \quad (44)$$

where k is the Boltzmann constant, T the absolute temperature, Ω the activation volume, and σ_I the normal stress supported by individual asperities. An increasing a value with temperature has been observed in previous experiments (e.g., Blanpied et al., 1998; He et al., 2013). When shear deformation falls in the intermediate-velocity regime (with high porosities and small ψ values), especially near the critical state

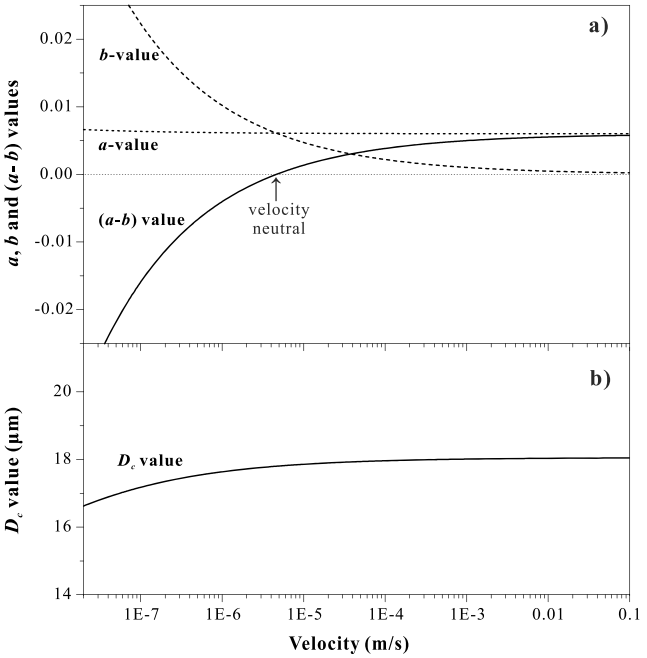

Figure 12. Values of (a) a, b, and $(a - b)$ and (b) D_c as a function of sliding velocity. The results are calculated from parameters that are chosen for a carbonate fault gouge and assuming pressure solution to be the contact creep mechanism. In general, the same trends are expected to be applicable for any granular material (e.g., calcite or quartz rich fault gouges) subjected to hydrothermal conditions.

that gives $\psi \approx 0$ (Figure 3), the expression for the direct effect reduces to $a \approx a_{\tilde{\mu}}$, which is consistent with previous interpretations of the direct effect (e.g., Beeler et al., 2007; Dieterich, 1979; Nakatani, 2001; Rice et al., 2001), except that the asperity stress σ_I is not necessarily a constant in our model. This suggests that the previous definition of the a value may be a subset of our more general expression, thus allowing to isolate the potential importance of the geometrical effect on the instantaneous contact strength. Indeed, as shear strain rate decreases, the gouge tends to be more compacted and thus has a high ψ value (and a low porosity). In this case, the direct effect would be promoted by dilatancy (Figure 12a). In other words, for a shearing gouge in the frictional regime with low porosity, the direct effect will be larger at a lower velocity due to the geometric effect. This trend has been recently observed by Takahashi et al. (2017) on halite-muscovite mixture gouges at room temperature (see their Figure 5). For carbonate gouge at the simulated conditions, porosity is at a relatively high level, so that the a value is not sensitive to velocity.

6.2.1.1. Evolution Effect (b Value)

The b value in our model is expressed as $b = b_\psi \frac{(1+\tilde{\mu}_{ss}^{\,2})}{(1-\tilde{\mu}_{ss}\hat{\mu}_{ss})^2}$, where b_ψ is the logarithmic rate dependence of the dilatant friction coefficient: $b_\psi \equiv \frac{\partial \hat{\mu}}{\partial(\ln V)}$. Again, the b value can be obtained by differentiating the general friction law; that is,

$$b = \frac{\partial \mu}{\partial(\ln V)}\Big|_{(V=V_{ss}^1)} = \frac{\partial \mu}{\partial \hat{\mu}}\frac{\partial \hat{\mu}}{\partial(\ln V)} = b_\psi \frac{(1+\tilde{\mu}_{ss}^{\,2})}{(1-\tilde{\mu}_{ss}\hat{\mu}_{ss})^2}. \quad (45)$$

The expressions for a and b are in the conjugated form (cf. equations (43) and (45)). Similarly, the evolution effect is controlled by b_ψ and also affected by grain boundary sliding. The most distinct difference between these two effects is that the evolution effect (b value) has variable, negative rate dependence while the direct effect (a value) has a nearly constant rate dependence (Figure 12a). Moreover, with increasing slip rates, the gouge will approach the critical state of granular flow ($\psi = 0$), at which the evolution effect would disappear.

6.2.1.2. Critical Slip Distance (D_c Value)

One major difference between the RSF laws and our microphysical model involves the length scale for state evolution D_c. The length scale in RSF laws is interpreted to be related to the average lifetime of a population of asperity sizes and as such has often been related to the size of asperities contacts (Dieterich, 1981; Sammis & Biegel, 1989). This interpretation gives a D_c that is independent of the slip rate unless velocity-dependent grain size reduction and/or de/localization is invoked. The length scale in our model is defined as the critical slip distance associated with the evolution of gouge state (i.e., porosity) in response to a small perturbation to the system (e.g., Sleep, 1997). As given by the theoretical expression derived (equations (38a) and (38b)), D_c is proportional to the shear zone thickness (e.g., Marone & Kilgore, 1993) and varies only slightly with driving velocity due to rate dependence of steady state porosity (Figure 12b).

6.2.1.3. Friction Rate Dependence ($a - b$)

The steady state friction rate dependence, $(a - b)$, is given by the difference between the a and b values. The sign of $(a - b)$ is determined by the competition between the velocity strengthening of grain boundary sliding and velocity weakening of dilatant granular flow. Based on their distinct sensitivities to strain rate as discussed above, our model would predict an increase of $(a - b)$ with increasing velocity (Figure 12a). Theoretically, this will lead to a transition from velocity-weakening ($a < b$), via neutral ($a = b$), to velocity-strengthening ($a > b$) behavior as velocity increases, for any granular fault gouge. At relatively high slip rates where $\psi \approx 0$, we have $(a - b) \approx a \approx a_{\tilde{\mu}}$. In this case, friction is entirely controlled by grain boundary sliding, giving rise to a logarithmic rate-strengthening behavior (see the dashed line in Figure 4a).

The above interpretations of RSF parameters are based on the assumption of an infinitesimally small velocity perturbation to a fault system. In fact, the apparent direct and evolution effects predicted by the CNS model

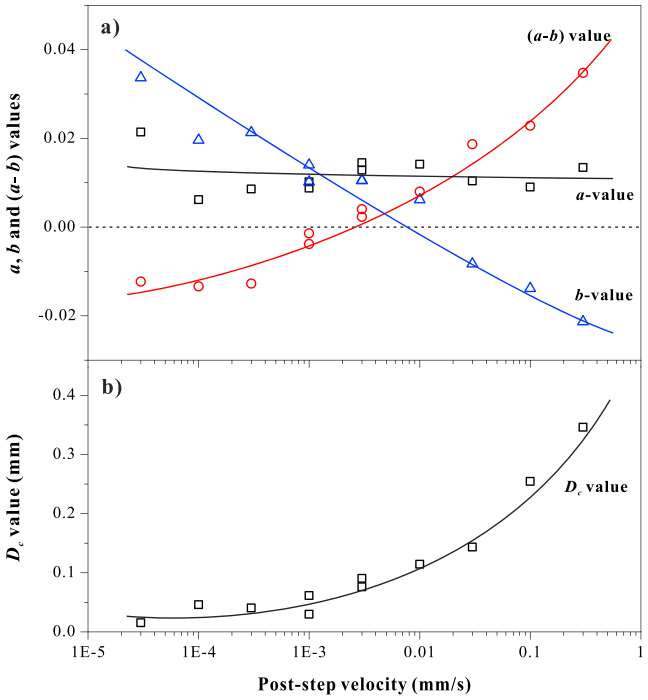

Figure 13. Representative experimental data showing the variations of (a) a, b, and ($a - b$) and (b) D_c with sliding velocity. The results were obtained for the principal slip zone gouge of the Alpine Fault that was sheared under hydrothermal conditions (150°C and 90 MPa effective normal stress, Niemeijer et al., 2016). The RSF parameters were extracted by inverse RSF modeling of the frictional curves with the slowness law. In some cases, two state variables provide a better data fit, for which we report the summed values for b and D_c. The solid lines give the interpreted trends of individual parameters. Results from the slowest velocity step ($3 \times 10^{-6} \rightarrow 1 \times 10^{-5}$ mm/s) are not shown due to the poor quality.

for large perturbations (e.g., a large velocity step) depend not only on sliding velocity but also on the size of the perturbation (Figure 7a). The equivalent slip(-weakening) distances d_0 also show an increasing trend with the magnitude of the velocity step (V^1/V^0) and differ between upstep and downstep of the same size (Figures 9 and 10).

6.3. Comparison With Experiments and Implications for Natural Faults

6.3.1. On the Friction Rate Dependence, a, b, and ($a - b$) Values

The transition from negative to positive rate dependence as shear strain rate increases in the intermediate velocity regime (*Crossover I* in Figure 3) has been reported for a wide variation of granular materials and conditions: (1) halite (Buijze et al., 2017; Shimamoto, 1986), clay-rich gouges (Ferri et al., 2011), glass polymer (poly(methyl methacrylate)), and glass beads (Bureau et al., 2002; Kuwano et al., 2013) at room temperature and humidity conditions; (2) calcite (Weeks, 1993) at high temperature and dry conditions; (3) carbonate slip surfaces and cataclasites at room temperature and fluid saturated conditions (Carpenter et al., 2014); and (4) calcite or natural carbonate fault rocks (Chen et al., 2015; Verberne et al., 2015), muscovite-quartz mixture (den Hartog & Spiers, 2014), and natural clay-rich fault gouges (Niemeijer et al., 2016; Niemeijer & Vissers, 2014) at hydrothermal conditions. All of these studies suggest that this transition might be a generic feature of granular friction. As addressed above, our model provides a sensible rationale for this: the direct and evolution effects have varying shear strain rate sensitivities with opposite signs.

Although the variations of ($a - b$) with shear strain rate have been well documented in literature, rare studies have reported the full set of RSF parameters, as a function of slip velocity (e.g., Carpenter et al., 2015, 2014; Niemeijer et al., 2016; Niemeijer & Vissers, 2014). Figure 13 presents the results for the principal-slip-zone gouge of the Alpine fault (consisting of quartz, feldspar, and minor phyllosilicates and calcite) sheared at 150°C and 90 MPa effective normal stress (Niemeijer et al., 2016). Under these conditions, the gouge shows a transition from velocity weakening to velocity strengthening as sliding velocity increases over 4 orders of magnitude (see their Figure 7). The values of a, b, and D_c for all the velocity step tests are extracted by inverse RSF modeling of the friction curve with the Slowness law. The trends of the variations of these parameters with sliding velocity are at a satisfactory agreement with the model prediction (cf. Figures 12 and 13). Consistent, systematic variations of RSF parameters (a, b, and D_c), as well as the transition in friction rate dependence ($a - b$), with sliding velocity, were also observed on carbonate slip surfaces and cataclasites (both wafers and powdered samples) at room temperature and fluid-saturated conditions (Carpenter et al., 2014), on a simulated fault gouge derived from a natural evaporate formation (consisting of mainly anhydrite and carbonates) at 100°C hydrothermal conditions (Hunfeld et al., 2017), and, of course, on simulated carbonate fault gouge at 80°C hydrothermal conditions (Chen et al., 2015; Verberne et al., 2015), which are the basis of all the numerical implementation in the present study.

Decreasing b value and nearly constant a value with increasing velocity (Figure 12a) have been widely observed for various gouge materials, typically for synthetic and natural clay-rich fault gouges deformed at low temperatures and wet conditions (e.g., the San Andreas Fault gouge, Carpenter et al., 2015, and the Longmenshan fault gouge, Chen et al., 2015). Within the laboratory velocity range, these materials almost exclusively show velocity-strengthening behavior (Ikari et al., 2011). However, as revealed by recent studies (e.g., den Hartog & Spiers, 2014; Lu & He, 2014; Zhang & He, 2016), as temperature increases, the phyllosilicate-rich gouge materials will undergo a transition from velocity strengthening to velocity weakening, at which point a similar transition with respect to varying velocity would also be observed (cf. Figure 13, Niemeijer et al., 2016). Some of these aspects have already been predicted by the steady state model proposed by den Hartog and Spiers (2014), but they need extending to the transient case.

Trends in RSF parameters that seem to be not consistent with the CNS model have been quite often observed as well. In many experiments, especially those performed on dry gouge materials or wet ones at low temperatures (e.g., Marone, 1998; Rathbun & Marone, 2013), the frictional behavior observed commonly shows a positive rate dependence over a wide range of slip rates, and the RSF parameters derived do not show drastic variations with slip rate where predicted by the CNS model (Figure 12). Some experiments even show the evolution of RSF parameters with cumulative displacement (Beeler et al., 1996) or slip localization (Leeman et al., 2016). It is noteworthy that the implementation of the CNS model in this study is based on the previous model for a calcite gouge sheared at conditions where the creep rate is relatively fast (Chen & Spiers, 2016). In principle, since independent experimental data suggest that similar elementary deformation processes will be active then the present model should be applicable to quartz gouges under hydrothermal conditions. One of the key issues in the model application lies in the kinetics of the contact creep mechanism for different materials. For wet quartz, the pressure solution rate is much slower compared with calcite at otherwise the same conditions (Spiers et al., 2004). According to the steady state solution (Table 1), lower $\tan\psi$ would be predicted, which will make the transition velocities, as now shown in Figures 3 and 4 for calcite, shift toward lower values, as well as causing the transition from velocity strengthening to weakening with increasing temperature to shift to a higher temperature. This prediction is consistent with existing laboratory data, that is, the transition temperature is ~300°C for quartz-rich gouges versus ~80°C for calcite (Blanpied et al., 1995; Chen et al., 2015; Chester & Higgs, 1992; Verberne et al., 2015). It can also explain why wet quartz gouge experiments predominantly show velocity-strengthening behavior at lower temperatures and laboratory slip rates (i.e., $<$200°C and 10^{-7}–10^{-4} m/s). For dry quartz, the CNS model would suffer more from uncertainties since either the intergranular creep mechanism or the stress concentration at contacts (the M value) is poorly constrained. Presumably, compaction in a dry gouge is much less efficient than in a wet one, such that even smaller $\tan\psi$ would be predicted, giving a steady state that is closer to the critical state of granular flow. In this case, as predicted by the CNS model, the deformation will be well in the velocity-strengthening regime, with RSF parameters that are insensitive to sliding velocity (see the inclined dash line in Figure 4). Albeit with the fact that this is a broad expectation only and validation for these conditions is difficult at present, this prediction is generally consistent with the common recognition of the rate dependence of dry (quartz) gouges in previous experiments (Marone, 1998). Finally, in the present study, an invariant shear band is assumed (constant λ value). However, it is also possible to consider variable shear band thickness (slip de/localization) in the CNS model. Based on the friction-velocity profile predicted (Figure 3), slip de/localization will cause variations in the friction rate dependence, as observed in experiments (e.g., Beeler et al., 1996). Moreover, based on the D_c expression derived, slip localization will cause a decrease in D_c and thus an increase in critical stiffness. Consequently, this will potentially destabilize the frictional behavior according to the classical fault stability theory (Scholz, 2002), which is consistent with experimental observations (e.g., Leeman et al., 2016).

In many experiments, varying a value with slip rate has been observed, which also can affect the overall picture of $(a-b)$ (e.g., Ikari et al., 2009; Takahashi et al., 2017). This is also inconsistent with the prediction by the CNS model (Figure 12). Recall that in the present model, intergranular flow (slip) and contact creep are considered to be dominant deformation mechanisms and that the direct effect is explained as the positive rate dependence of grain boundary friction. However, other micromechanical processes such as grain size reduction, cohesion, and slip de/localization can also contribute to or moderate the instantaneous response of a fault, thereby changing the a value and the overall friction rate dependence. Moreover, from the derived expression for $a_{\tilde{\mu}}$ (equation (44)), the direct effect depends on local stress at contact asperities σ_I which may also vary with the slip velocity (e.g., Takahashi et al., 2017). Another possibility to explain the inconsistency is that the shear deformation is not in the intermediate-velocity friction regime such that the expressions derived in the present study do not apply anymore (Figure 3). In other regimes, other effects such as plastic flow and frictional heating need to be incorporated (Elbanna & Carlson, 2014; Noda, 2008). Additional notes on these aspects will be addressed in section 6.4.

As applied to natural faults, the a value is expected to increase as temperature increases, being more or less proportional to the absolute temperature. With increasing depth, the effective normal stresses acting on the grain contacts are also expected to increase, which will exert an opposite effect on the a value. The b value, being proportional to the average dilatancy angle, is controlled by the contact creep law and the slip rate imposed on the fault (equation (13)). Generally, an increase in temperature will enhance creep and thus the compaction process, leading to larger evolution effects. Due to the different sensitivities of a and b

with respect to temperature (and pressure), their combination will give rise to a transition from velocity strengthening to velocity weakening with increasing depth. As the fault goes deeper and enters the flow regime, it will turn back to velocity strengthening. Unlike the classical RSF laws in which the parameters are usually taken as constants, our model predicts the equivalent a and b values that vary with sliding velocity (also with other factors such as temperature, depth, and fault zone structure). If we consider a dynamic loading process within a seismic cycle, the slip velocity of a fault will fall in a broad range from plate velocity (nm/s) to meters per second. According to our model, the seismogenic zone, with $(a-b)<0$, would experience spatial and temporal variations within a seismic cycle. This warrants numerical simulations of earthquake cycles with our CNS model to be done in the future.

6.3.2. On the Critical and Equivalent Slip (-Weakening) Distance: D_c Versus d_0

Our results show that the critical slip distance D_c depends weakly on slip rate due to the rate-dependent porosity but not on the size or the sign of velocity steps (Figures 7b and 12b). This is in general consistent with the previous recognition in the framework of classical RSF laws or pure slip-weakening laws (Scholz, 2002). Slight, systematic variations of critical slip distance with slip rate have been observed in previous experiments involving granular fault gouges. Mair and Marone (1999) performed frictional experiments in quartz gouge over a wide range of velocities and found a slight decrease in D_c value with decreasing sliding velocity, consistent with the prediction from our model. As addressed earlier in this section, similar changes in D_c were also seen in other granular gouge materials (e.g., Buijze et al., 2017; Carpenter et al., 2014; Hunfeld et al., 2017; Niemeijer et al., 2016). Recently, large velocity step experiments have been performed on different quartz gouges over a wide range of slip rates (Bhattacharya et al., 2015; Rathbun & Marone, 2013) and the results showed that the Slip law can well explain the experiments across a few orders of magnitude variations in slip rate and step size. By inversely fitting the frictional curves, these authors also found that D_c is indeed a characteristic distance that is independent of either the size or the sign of the velocity steps over a wide range of slip rates.

Previous estimates of the critical displacement length for natural faults range over several orders of magnitude (e.g., Abercrombie & Rice, 2005). Measurements of D_c in the lab are thought to scale up to natural seismogenic faults, which usually have wider incohesive gouge zones and higher roughness. Abercrombie and Rice (2005) argued that the D_c values for local regions of a fault zone could be on the same scale as the measurements from laboratories (0.01 to 0.1 mm), but thicker and rougher patches may require larger shear displacement (0.5 mm) to instigate breakdown of strength. Ohnaka (2003) also proposed that D_c is associated with the roughness of the fault plane (sliding surface), which to some extent suggests that the scale of the macroscopic description of fault friction corresponds to the thickness of the principal slip zone. An estimate of the D_c value for a small fault in a deep gold mine in South Africa is 0.1 mm, and it was suggested that D_c scales with the thickness of the gouge zone (Richardson & Jordan, 2002). This argument is supported by the laboratory study by Marone and Kilgore (1993), who observed a significant reduction in D_c with shear localization. Based on their observations, an empirical formula that scales D_c with shear band thickness ($L_t\lambda$) was proposed; that is,

$$D_c = \zeta \cdot (L_t \lambda), \tag{46}$$

where ζ is a constant factor inferred to be ~0.01 from their experiments. Here our theoretical analysis gives a physics-based expression linking D_c with shear band thickness (Table 2). This is consistent with the interpretations from the previous experiments (Beeler et al., 1996; Dieterich, 1981; Ito & Ikari, 2015; Marone & Kilgore, 1993; Rathbun & Marone, 2013; Richardson & Jordan, 2002).

Since D_c characterizes the length scale for a transient frictional behavior, it is expected to be related to the geometric attributes of a fault system, such as gouge particle size and sliding surface roughness. Indeed, previous experiments revealed that the length of D_c correlates with the average grain size for granular fault gouges (Dieterich, 1981; Marone & Kilgore, 1993; Sammis & Biegel, 1989). It is hypothesized that in granular materials, shear usually localizes into discrete zones that are typically several to 20 particles thick (e.g., Rathbun & Marone, 2010). This hypothesis was supported by the dilatation/compaction measurements that revealed that for the same velocity step, greater changes in layer thickness occur in the larger grain-sized gouge layers (e.g., Rathbun & Marone, 2013; Samuelson et al., 2011). In other words, the larger the grain size, the more the absolute dilatation/compaction is, the thicker the actual slip zone will be. Therefore, the correlation of D_c with particle size is in some sense consistent with our scaling relation between D_c with slip zone

thickness. In addition, friction of simulated gouge layers generally exhibits larger D_c values than that of initially bare surfaces (e.g., Marone et al., 1990; see a data set compiled by Paterson & Wong, 2005, referring to the first length D_{c1} only). This difference can be explained by our model considering the fact that gouge material is produced by wearing of bare rock surfaces and that a simulated gouge layer generally has a larger thickness (>1 mm). The influence of roughness of the rock surfaces was demonstrated by Dieterich (1979) and Okubo and Dieterich (1984) who observed an increase of the D_c value with increasing roughness of the granodiorite and granite surfaces. Again, this effect can be predicted by our model in view of the fact that shear is prone to be localized along or near the boundary (Chester et al., 1993).

Overall, the predicted variations of D_c with slip rate and slip zone thickness (gouge grain size and surface roughness) by our model are consistent with previous laboratory results. This suggests that the microphysical model may capture important behavior for gouge-filled faults, which is all absent in the RSF laws. Considering the irregularity of natural slip surfaces and the fact that the displacement rates and accelerations involved in a natural earthquake may vary over several orders of magnitude during nucleation, propagation, and arrest of an earthquake rupture process, the critical slip distance can, therefore, vary significantly. The variable length scale in the model thus has a potentially larger impact than in the RSF laws. Simply using parameters from our lab experiments, our model, however, predicts a larger proportional factor in the scaling law of about 0.3 (equation (46), using H of 1 and φ_{ss} of 0.18). Applying this to natural faults, for example, to the San Andreas Fault, which has a slip band thickness of ~10 cm (Chester et al., 1993), our model predicts a minimum characteristic slip distance of ~2.4 cm. In conclusion, we thus propose that our model might offer an alternative explanation for the discrepancy between the lab- and field-based measurements of D_c as well as a potential method for scaling between the two.

In contrast with the critical slip distance, d_0, the equivalent slip (-weakening) distance in response to large perturbations, as given in equation (38a) or (42a) or (B13) in supporting information, does depend on the velocity perturbation size. Recall that Bhattacharya et al. (2015) found that the same D_c value can apply to velocity steps with varying slip rates and sizes over a few orders of magnitude, provided that a proper friction law is used. However, without fitting the data, it is also apparent in their frictional curves that the slip-weakening distance (d_0 values) increases drastically with the velocity perturbation sizes, and the upstep and downstep behave roughly symmetrically (see their Figure 2, for instance). Van den Ende et al. (2015) have more recently performed similar experiments on halite, and they also observed a systematic increase in d_0 with increasing stepping size. Different from the quartz experiments, these authors found systematically larger slip distances in the upsteps than the downsteps of the same size. Finally, a similar trend of D_c varying with the sign and size of V^1/V^0 was also observed for our carbonate fault gouge (Chen et al., 2015). All of these behaviors are generally consistent with the prediction by the CNS model (Figure 10), except the symmetric behavior observed for dry quartz. We infer that this might be attributed to the fact that the RSF parameters of a dry gouge are insensitive to slip rates, which, as addressed earlier, can also be promisingly predicted by the model.

6.4. Additional Notes, Limitations, and Future Work

One would like to use the lab-derived RSF parameters to model earthquake dynamics. However, without being aware of the underlying physics, extrapolation of these empirical parameters to natural seismogenic conditions should be done with caution. In this study, physical expressions for RSF parameters are derived from a microphysical model, providing a more reliable basis to address this issue. In addition to the points discussed above, we have the following notes on the general applicability of our model.

First, to derive these expressions, large wall rock stiffness has been assumed. This is plausible in dealing with laboratory faults where the "wall rocks" are usually simulated by steel or intact rocks. However, the stiffness of natural fault zones can vary by several orders of magnitude, which may play a significant role in determining the frictional strength and stability of the fault. Second, the load point velocities in laboratory experiments are usually in the order of μm/s, which is 3–5 orders of magnitude higher than that in the nucleation phase of a natural earthquake (of the order of typical plate velocity of 10^{-9} m/s), such that the $(a - b)$ values obtained cannot be directly applied to natural fault zones. As the slip rate decreases, nondilatant plastic creep would become dominant, leading to a transition in the steady state frictional/flow stress (*Crossover II* in Figure 3). The transition from friction to plastic flow as strain rate decreases has been reported in quartz (Chester & Higgs, 1992), halite (Buijze et al., 2017; Miao et al., 2012; Shimamoto, 1986), halite-phyllosilicate (Bos & Spiers, 2002;

Buijze et al., 2017), and serpentine gouges (Moore et al., 1997). Caution should also be taken when extrapolating to high slip rates, where mechanisms activated by frictional heating are expected to be dominant, causing a transition to dynamic slip weakening (Noda, 2008).

Second, our model, with porosity as the state variable, is consistent with the classical theory of RSF laws, which infers that the change in contact area determines the evolutional frictional strength (Dieterich, 1979). As the shear velocity increases, the gouge must dilate, causing an increase in porosity and thus a decrease in the contact area (Figure 2). Consequently, this will lead to lower frictional resistance to contact sliding and hence a velocity-weakening process. In fact, this behavior is a reflection of the fact that contacts do not have time to grow by contact creep as shear velocity increases, so in this sense, the evolution effect in our model is related to contact lifetime similar to that proposed in the context of RSF laws.

We further note that in laboratory faults, velocity weakening is not usually observed until strain localizes to a narrow shear band. In the present model, we prescribe a slip localization to the fault gouge layer and do not allow it to evolve. We assume no inertia for the purpose to grasp the physics underpinning the equations. All these effects need to be incorporated into the model (e.g., Rice & Tse, 1986; Sleep et al., 2000). Our model can capture the friction behavior of a gouge-filled fault on the laboratory scale. At the scale of natural faults, the friction laws control the complexity of individual ruptures. Therefore, applying the CNS model in the context of the cycling of earthquake rupture can help determine how the macroscopic observations can be affected by the fault constitutive parameters as well as their temporal and spatial variations.

Finally, having the expressions for $(a - b)$ and D_c, we can calculate the critical stiffness K_c that delineates the slip stability fields of a potentially seismogenic fault, represented as a spring-slider system, which is given as $K_c = (b - a)\sigma_n/D_c$ (Rice & Ruina, 1983). Inserting our physical expressions for a, b, and D_c into this equation, we get a stability criterion that is identical to the one that we obtained independently using linear perturbation analysis directly on the microphysical model (see the companion paper).

7. Conclusions

In a recent paper, a microphysical model was presented that describes the frictional behavior of a carbonate fault gouge, with pressure solution and granular flow being the deformation mechanisms at the simulated conditions of pressure and temperature (Chen & Spiers, 2016). The present work starts with a general model of granular friction in which intergranular flow and creep on grain contacts are taken to be the dominant mechanisms accommodating sample deformation. By analytically solving the constitutive equations, expressions for the steady state frictional strength and standard RSF parameters, that is, a, b, and D_c, have been obtained (summarized in Table 1).

1. The frictional strength of a granular material (μ) consists of two components, namely, the grain boundary frictional strength ($\widetilde{\mu}$) and the frictional strength due to intergranular dilatation ($\hat{\mu} \equiv \tan\psi$).
2. The direct and evolutional parameters a and b can be expressed in a conjugate form, that is, $a = a_{\widetilde{\mu}} \frac{(1+\hat{\mu}^2)}{(1-\hat{\mu}\widetilde{\mu})^2}$ and $b = b_\psi \frac{(1+\widetilde{\mu}^2)}{(1-\hat{\mu}\widetilde{\mu})^2}$, where $a_{\widetilde{\mu}}$ and b_ψ are the logarithmic rate dependences of $\widetilde{\mu}$ and $\hat{\mu}$, respectively.
3. The model predicts a critical slip distance D_c that scales with slip band thickness and varies only slightly with slip velocity, while d_0, the equivalent slip distance in response to large perturbations, increases with the velocity perturbation size.

The values of a, b, and D_c predicted by these expressions agree well with the numerical modeling results and reasonably well with those obtained from experiments performed at similar conditions. Using the parameters obtained, the forward modeling employing classical RSF laws (Slowness and Slip laws) gives results that are fully consistent with the predictions from the CNS model for small departures from steady state. The predicted scaling law for D_c is in-line with previous lab experiments and geophysical observations in natural faults, potentially explaining the discrepancies between seismological and experimental observations. In a companion paper, we investigate the slip stability of the model, giving the microphysical interpretation of critical stiffness, which is consistent with the result calculated from $K_c = (b - a)\sigma_n/D_c$. All of these testify to the validity of the expressions obtained in the present study.

Considering the consistency between these expressions and the previous interpretations of the parameters obtained in the context of RSF laws, our mechanism-based model can provide a physical basis for extrapolating the lab-derived parameters to natural seismogenic conditions. In future work, we plan to investigate the model under variable conditions, that is, variable normal stress, and also to apply the model to earthquake rupture modeling.

Acknowledgments
We thank the Associate Editor Y. Kaneko and two anonymous reviewers for unusually detailed and insightful reviews. Jianye Chen is funded by the European Research Council starting grant SEISMIC (335915). André Niemeijer is funded by SEISMIC (335915) and the Netherlands Organization for Scientific research (NWO) VIDI grant (854.12.011). This is a theoretical paper, and it does not contain any data.

References

Abercrombie, R. E., & Rice, J. R. (2005). Can observations of earthquake scaling constrain slip weakening? *Geophysical Journal International*, *162*, 406–424. https://doi.org/10.1111/j.1365-246X.2005.02579.x

Aki, K. (1987). Magnitude-frequency relation for small earthquakes: A clue to the origin of f_{max} of large earthquakes. *Journal of Geophysical Research*, *21*(18), 1987–1990. https://doi.org/10.1029/94GL01599

Ampuero, J.-P., & Rubin, A. M. (2008). Earthquake nucleation on rate-and-state faults: Aging and slip laws. *Journal of Geophysical Research*, *113*, B01302. https://doi.org/10.1029/2007JB005082

Barbot, S., Fialko, Y., & Bock, Y. (2009). Postseismic deformation due to the M_w 6.0 2004 Parkfield earthquake: Stress driven creep on a fault with spatially variable rate-and-state friction parameters. *Journal of Geophysical Research*, *114*, B07405. https://doi.org/10.1029/2008JB005748

Bar-Sinai, Y., Spatschek, R., Brener, E. A., & Bouchbinder, E. (2014). On the velocity-strengthening behavior of dry friction. *Journal of Geophysical Research: Solid Earth*, *119*, 1738–1748. 10.1002/2013JB010586

Baumberger, T., Berthoud, P., & Caroli, C. (1999). Physical analysis of the state- and rate-dependent friction law. II. Dynamic friction. *Physical Review B*, *60*(6), 3928–3939. https://doi.org/10.1103/PhysRevB.60.3928

Baumberger, T., & Caroli, C. (2006). Solid friction from stick–slip down to pinning and aging. *Advances in Physics*, *55*(3–4), 279–348. https://doi.org/10.1080/00018730600732186

Beeler, N. M., Tullis, T. E., Blanpied, M. L., & Weeks, J. D. (1996). Frictional behavior of large displacement experimental faults. *Journal of Geophysical Research*, *101*(B4), 8697–8715. https://doi.org/10.1029/96JB00411

Beeler, N. M., Tullis, T. E., & Goldsby, D. L. (2008). Constitutive relationships and physical basis of fault strength due to flash heating. *Journal of Geophysical Research*, *113*, B01401. https://doi.org/10.1029/2007JB004988

Beeler, N. M., Tullis, T. E., Kronenberg, A. K., & Reinen, L. A. (2007). The instantaneous rate dependence in low temperature laboratory rock friction and rock deformation experiments. *Journal of Geophysical Research*, *112*, B07310. https://doi.org/10.1029/2005JB003772

Beeler, N., Tullis, T. E., & Weeks, J. D. (1994). The roles of time and displacement in the evolution effect in rock friction. *Geophysical Research Letters*, *21*(18), 1987–1990. https://doi.org/10.1029/94GL01599

Berthoud, P., Baumberger, T., G'Sell, C., & Hiver, J.-M. (1999). Physical analysis of the state- and rate-dependent friction law: Static friction. *Physical Review B*, *59*(22), 14,313–14,327. https://doi.org/10.1103/PhysRevB.59.14313

Bhattacharya, P., & Rubin, A. M. (2014). Frictional response to velocity steps and 1-D fault nucleation under a state evolution law with stressing-rate dependence. *Journal of Geophysical Research: Solid Earth*, *119*, 2272–2304. https://doi.org/10.1002/2013JB010671

Bhattacharya, P., Rubin, A. M., Bayart, E., Savage, H. M., & Marone, C. (2015). Critical evaluation of state evolution laws in rate and state friction: Fitting large velocity steps in simulated fault gouge with time-, slip-, and stress-dependent constitutive laws. *Journal of Geophysical Research: Solid Earth*, *120*, 6365–6385. https://doi.org/10.1002/2015JB012437

Bizzarri, A., & Cocco, M. (2003). Slip-weakening behavior during the propagation of dynamic ruptures obeying rate- and state-dependent friction laws. *Journal of Geophysical Research*, *108*(B8), 2373. https://doi.org/10.1029/2002JB002198

Blanpied, M. L., Lockner, D. A., & Byerlee, J. D. (1995). Frictional slip of granite at hydrothermal conditions. *Journal of Geophysical Research*, *100*(B7), 13,045–13,064. https://doi.org/10.1029/95JB00862

Blanpied, M. L., Marone, C. J., Lockner, D. A., Byerlee, J. D., & King, D. P. (1998). Quantitative measure of the variation in fault rheology due to fluid-rock interactions. *Journal of Geophysical Research*, *103*(B5), 9691–9712. https://doi.org/10.1029/98JB00162

Bos, B., & Spiers, C. J. (2002). Fluid-assisted healing processes in gouge bearing faults: Insights from experiments on a rock analogue system. *Pure and Applied Geophysics*, *159*(11–12), 2537–2566. https://doi.org/10.1007/s00024-002-8747-2

Buijze, L., Niemeijer, A., Han, R., Shimamoto, T., & Spiers, C. J. (2017). Friction properties and deformation mechanisms of halite(-mica) gouges from low to high sliding velocities. *Earth and Planetary Science Letters*, *458*, 107–119. https://doi.org/10.1016/j.epsl.2016.09.059

Bureau, L., Baumberger, T., & Caroli, C. (2002). Rheological aging and rejuvenation in solid friction contacts. *European Physical Journal E*, *8*(3), 331–337. https://doi.org/10.1140/epje/i2002-10017-1

Carpenter, B. M., Saffer, D. M., & Marone, C. (2015). Frictional properties of the active San Andreas Fault at SAFOD: Implications for fault strength and slip behavior. *Journal of Geophysical Research: Solid Earth*, *120*, 5273–5289. https://doi.org/10.1002/2015JB011963

Carpenter, B. M., Scuderi, M. M., Collettini, C., & Marone, C. (2014). Frictional heterogeneities on carbonate-bearing normal faults: Insights from the Monte Maggio Fault, Italy. *Journal of Geophysical Research: Solid Earth*, *119*, 9062–9076. https://doi.org/10.1002/2014JB011337

Chen, J., & Niemeijer, A. R. (2017). Seismogenic potential of a gouge-filled fault and the criterion for its slip stability: Constraints from a microphysical model. *Journal of Geophysical Research: Solid Earth*, *122*, 9658–9688. https://doi.org/10.1002/2017JB014228

Chen, J., & Spiers, C. J. (2016). Rate and state frictional and healing behavior of carbonate fault gouge explained using microphysical model. *Journal of Geophysical Research: Solid Earth*, *121*, 8642–8665. https://doi.org/10.1002/2016JB013470

Chen, J., Verberne, B. A., & Spiers, C. J. (2015). Effects of healing on the seismogenic potential of carbonate fault rocks: Experiments on samples from the Longmenshan Fault, Sichuan, China. *Journal of Geophysical Research: Solid Earth*, *120*, 5479–5506. https://doi.org/10.1002/2015JB012051

Chen, T., & Lapusta, N. (2009). Scaling of small repeating earthquakes explained by interaction of seismic and aseismic slip in a rate and state fault model. *Journal of Geophysical Research*, *114*, B01311. https://doi.org/10.1029/2008JB005749

Chester, F. M. (1994). Effects of temperature on friction: Constitutive equations and experiments with fault gouge. *Journal of Geophysical Research*, *99*(B4), 7247–7261. https://doi.org/10.1029/93JB03110

Chester, F. M., Evans, J. P., & Biegel, R. L. (1993). Internal structure and weakening mechanisms of the San Andreas Fault. *Journal of Geophysical Research*, *98*(B1), 771–786. https://doi.org/10.1029/92JB01866

Chester, F. M., & Higgs, N. G. (1992). Multimechanism friction constitutive model for ultrafine quartz gouge at hypocentral conditions. *Journal of Geophysical Research*, *97*(B2), 1859–1870. https://doi.org/10.1029/91JB02349

Daub, E. G., & Carlson, J. M. (2008). A constitutive model for fault gouge deformation in dynamic rupture simulations. *Journal of Geophysical Research*, *113*, B12309. https://doi.org/10.1029/2007JB005377

Di Toro, G., Han, R., Hirose, T., De Paola, N., Nielsen, S., Mizoguchi, K., … Shimamoto, T. (2011). Fault lubrication during earthquakes. *Nature*, *471*, 493–499.

Dieterich, J. H. (1978). Time-dependent friction and the mechanics of stick-slip. *Pure and Applied Geophysics*, *116*(4–5), 790–806. https://doi.org/10.1007/BF00876539

Dieterich, J. H. (1979). Modeling of rock friction: 1. Experimental results and constitutive equations. *Journal of Geophysical Research*, *84*(B5), 2161–2168. https://doi.org/10.1029/JB084iB05p02161

Dieterich, J. H. (1981). Constitutive properties of faults with simulated gouge. In N. L. Carter, et al. (Eds.), *Mechanical behavior of crustal rocks*, *Geophysical Monograph Series* (Vol. 24, pp. 103–120). Washington, DC: American Geophysical Union. https://doi.org/10.1029/GM024p0103

Dieterich, J. H. (1986). A model for the nucleation of earthquake slip. In S. Das, J. Boatwright, & C. H. Scholz (Eds.), *Earthquake source mechanics*, *Geophysical Monograph Series* (Vol. 37, pp. 37–47). Washington, DC: American Geophysical Union.

Dieterich, J. H. (1992). Earthquake nucleation on faults with rate and state dependent strength. *Tectonophysics*, *211*(1–4), 115–134. https://doi.org/10.1016/0040-1951(92)90055-B

Dieterich, J. H. (1994). A constitutive law for the rate of earthquake production and its application to earthquake clustering. *Journal of Geophysical Research*, *99*(B2), 2601–2618. https://doi.org/10.1029/93JB02581

Elbanna, A. E., & Carlson, J. M. (2014). A two-scale model for sheared fault gouge: Competition between macroscopic disorder and local viscoplasticity. *Journal of Geophysical Research: Solid Earth*, *119*, 4841–4859. https://doi.org/10.1002/2014JB011001

Estrin, Y., & Bréchet, Y. (1996). On a model of frictional sliding. *Pure and Applied Geophysics*, *147*(4), 745–762. https://doi.org/10.1007/BF01089700

Ferri, F., Di Toro, G., Hirose, T., Han, R., Noda, H., Shimamoto, T., … de Rossi, N. (2011). Low- to high- velocity frictional properties of the clay-rich gouges from the slipping zone of the 1963 Vaiont slide, northern Italy. *Journal of Geophysical Research*, *116*, B09208. https://doi.org/10.1029/2011JB008338

den Hartog, S. A. M., & Spiers, C. J. (2013). Influence of subduction zone conditions and gouge composition on frictional slip stability of megathrust faults. *Tectonophysics*, *600*, 75–90. https://doi.org/10.1016/j.tecto.2012.11.006

den Hartog, S. A. M., & Spiers, C. J. (2014). A microphysical model for fault gouge friction applied to subduction megathrusts. *Journal of Geophysical Research: Solid Earth*, *119*, 1510–1529. https://doi.org/10.1002/2013JB010580

Hatano, T. (2015). Rate and state friction law as derived from atomistic processes at asperities, doi:arXiv:1512.05078 [cond-mat.stat-mech].

Hawthorne, J. C., & Rubin, A. M. (2013). Laterally propagating slow slip events in a rate and state friction model with a velocity-weakening to velocity-strengthening transition. *Journal of Geophysical Research: Solid Earth*, *118*, 3785–3808. https://doi.org/10.1002/jgrb.50261

He, C., Luo, L., Hao, Q.-M., & Zhou, Y. (2013). Velocity-weakening behavior of plagioclase and pyroxene gouges and stabilizing effect of small amounts of quartz under hydrothermal conditions. *Journal of Geophysical Research: Solid Earth*, *118*, 3408–3430. https://doi.org/10.1002/jgrb.50280

Helmstetter, A., & Shaw, B. (2009). Afterslip and aftershocks in the rate-and-state friction law. *Journal of Geophysical Research*, *114*, B01308. https://doi.org/10.1029/2007JB005077

Heslot, F., Baumberger, T., Perrin, B., Caroli, B., & Caroli, C. (1994). Creep, stick-slip, and dry friction dynamics: Experiments and a heuristic model. *Physical Review E*, *49*(6), 4973–4988. https://doi.org/10.1103/PhysRevE.49.4973

Hetland, E. A., Simons, M., & Dunham, E. M. (2010). Post-seismic and interseismic fault creep I: Model description. *Geophysical Journal International*, *181*, 81–98. https://doi.org/10.1111/j.1365-246X.2010.04522.x

Hunfeld, L. B., Niemeijer, A. R., & Spier, C. J. (2017). Frictional properties of simulated fault gouges from the seismogenic Groningen gas field under in-situ P-T-chemical conditions. *Journal of Geophysical Research: Solid Earth*, *122*. https://doi.org/10.1002/2017JB014876

Ida, Y. (1973). The maximum acceleration of strong ground motion. *Bulletin of the Seismological Society of America*, *63*, 959–968.

Ide, S., & Takeo, M. (1997). Determination of constitutive relations of fault slip based on seismic wave analysis. *Journal of Geophysical Research*, *102*(B12), 27,379–27,391. https://doi.org/10.1029/97JB02675

Ikari, M. J., Carpenter, B. M., & Marone, C. (2016). A microphysical interpretation of rate- and state dependent friction for fault gouge. *Geochemistry, Geophysics, Geosystems*, *17*(5), 1660–1677. https://doi.org/10.1002/2016GC006286

Ikari, M. J., Marone, C., & Saffer, D. M. (2011). On the relation between fault strength and frictional stability. *Geology*, *39*, 83–86. https://doi.org/10.1130/G31416.1

Ikari, M. J., Saffer, D. M., & Marone, C. (2009). Frictional and hydrologic properties of clay-rich fault gouge. *Journal of Geophysical Research*, *114*, B05409. https://doi.org/10.1029/2008JB006089

Ito, Y., & Ikari, M. J. (2015). Velocity and slip-dependent weakening in simulated fault gouge: Implications for multimode fault slip. *Geophysical Research Letters*, *42*(21), 9247–9254. https://doi.org/10.1002/2015GL065829

Kaneko, Y., Fukuyama, E., & Hamling, I. J. (2017). Slip-weakening distance and energy budget inferred from near-fault ground deformation during the 2016 M_w7.8 Kaikoura earthquake. *Geophysical Research Letters*, *44*(10), 4765–4773. https://doi.org/10.1002/2017GL073681

Kato, N., & Tullis, T. E. (2001). A composite rate- and state-dependent law for rock friction. *Geophysical Research Letters*, *28*, 1103–1106. https://doi.org/10.1029/2000GL012060

Kuwano, O., Ando, R., & Hatano, T. (2013). Crossover from negative to positive shear rate dependence in granular friction. *Geophysical Research Letters*, *40*, 1295–1299. https://doi.org/10.1002/grl.50311

Lapusta, N., & Rice, J. R. (2003). Nucleation and early seismic propagation of small and large events in a crustal earthquake model. *Journal of Geophysical Research*, *108*(B4), 2205. https://doi.org/10.1029/2001JB000793

Leeman, J. R., Saffer, D. M., Scuderi, M. M., & Marone, C. (2016). Laboratory observations of slow earthquakes and the spectrum of tectonic fault slip modes. *Nature Communications*, *7*. https://doi.org/10.1038/ncomms11104

Lieou, C. K. C., Daub, E. G., Guyer, R. A., Ecke, R. E., Marone, C., & Johnson, P. A. (2017). Simulating stick-slip failure in a sheared granular layer using a physics-based constitutive model. *Journal of Geophysical Research: Solid Earth*, *122*, 295–307. https://doi.org/10.1002/2016JB013627

Linker, M. F., & Dieterich, J. H. (1992). Effects of variable normal stress on rock friction: Observations and constitutive equations. *Journal of Geophysical Research*, *97*(B4), 4923–4940. https://doi.org/10.1029/92JB00017

Liu, Y. J., & Rice, J. R. (2005). Aseismic slip transients emerge spontaneously in three-dimensional rate and state modeling of subduction earthquake sequences. *Journal of Geophysical Research*, *110*, B08307. https://doi.org/10.1029/2004JB003424

Liu, Y., & Rubin, A. M. (2010). Role of fault gouge dilatancy on aseismic deformation transients. *Journal of Geophysical Research*, *115*, B10414. https://doi.org/10.1029/2010JB007522

Lu, Z., & He, C. (2014). Frictional behavior of simulated biotite fault gouge under hydrothermal conditions. *Tectonophysics*, *622*, 62–80. https://doi.org/10.1016/j.tecto.2014.03.002

Mair, K., & Marone, C. (1999). Friction of simulated fault gouge for a wide range of velocities and normal stresses. *Journal of Geophysical Research*, *104*(B12), 28,899–28,914. https://doi.org/10.1029/1999JB900279

Marone, C. (1998). Laboratory–derived friction laws and their application to seismic faulting. *Annual Review of Earth and Planetary Sciences*, *26*(1), 643–696. https://doi.org/10.1146/annurev.earth.26.1.643

Marone, C., Cocco, M., Richardson, E., & Tinti, E. (2009). The critical slip distance for seismic and aseismic fault zones of finite width. In E. Fukuyama (Ed.), *Fault-Zone properties and earthquake rupture dynamics*, *International Geophysical Services* (Vol. 94, pp. 135–162). New York: International Geophysics, Academic Press. https://doi.org/10.1016/S0074-6142(08)00006-5

Marone, C., & Kilgore, B. (1993). Scaling of the critical slip distance for seismic faulting with shear strain in fault zones. *Nature*, *362*(6421), 618–621. https://doi.org/10.1038/362618a0

Marone, C., Raleigh, C. B., & Scholz, C. H. (1990). Frictional behavior and constitutive modeling of simulated fault gouge. *Journal of Geophysical Research*, *95*(B5), 7007–7025. https://doi.org/10.1029/JB095iB05p07007

Marone, C., Scholz, C. H., & Bilham, R. (1991). On the mechanics of earthquake afterslip. *Journal of Geophysical Research*, *96*(B5), 8441–8452. https://doi.org/10.1029/91JB00275

Marone, C., Vidale, J. E., & Ellsworth, W. (1995). Fault healing inferred from time dependent variations in source properties of repeating earthquakes. *Geophysical Research Letters*, *22*(22), 3095–98. https://doi.org/10.1029/95GL03076

Miao, A. L., Ma, S. L., Hou, L. F., & Yao, L. (2012). Velocity-dependence transition of friction for halite gouge and its significance implication in seismology [in Chinese with English abstract]. *Chinese Journal of Geophysics*, *55*, 3307–3317.

Mikumo, T., Olsen, K. B., Fukuyama, E., & Yagi, Y. (2003). Stress-breakdown time and slip-weakening distance inferred from slip-velocity functions on earthquake faults. *Bulletin of the Seismological Society of America*, *93*(1), 264–282. https://doi.org/10.1785/0120020082

Moore, D., Lockner, D., Shengli, M., Summers, R., & Byerlee, J. (1997). Strengths of serpentinite gouges at elevated temperatures. *Journal of Geophysical Research*, *102*(B7), 14,787–14,801. https://doi.org/10.1029/97JB00995

Nakatani, M. (1998). A new mechanism of slip-weakening and strength recovery of friction associated with the mechanical consolidation of gouge. *Journal of Geophysical Research*, *103*(B11), 27,239–27,256. https://doi.org/10.1029/98JB02639

Nakatani, M. (2001). Conceptual and physical clarification of rate and state friction: Frictional sliding as a thermally activated rheology. *Journal of Geophysical Research*, *106*(B7), 13,347–13,380. https://doi.org/10.1029/2000JB900453

Nakatani, M., & Scholz, C. H. (2004). Frictional healing of quartz gouge under hydrothermal conditions: 2. Quantitative interpretation with a physical model. *Journal of Geophysical Research*, *109*, B07202. https://doi.org/10.1029/2003JB002938

Niemeijer, A. R., Boulton, C., Toy, V. G., Townend, J., & Sutherland, R. (2016). Large-displacement, hydrothermal frictional properties of DFDP-1 fault rocks, Alpine Fault, New Zealand: Implications for deep rupture propagation. *Journal of Geophysical Research: Solid Earth*, *121*, 624–647. https://doi.org/10.1002/2015JB012593

Niemeijer, A., Di Toro, G., Nielsen, S., & Di Felice, F. (2011). Frictional melting of gabbro under extreme experimental conditions of normal stress, acceleration, and sliding velocity. *Journal of Geophysical Research*, *116*, B07404. https://doi.org/10.1029/2010JB008181

Niemeijer, A. R., & Spiers, C. J. (2006). Velocity dependence of strength and healing behaviour in simulated phyllosilicate-bearing fault gouge. *Tectonophysics*, *427*, 231–253. https://doi.org/10.1016/j.tecto.2006.03.048

Niemeijer, A. R., & Spiers, C. J. (2007). A microphysical model for strong velocity weakening in phyllosilicate-bearing fault gouges. *Journal of Geophysical Research*, *112*, B10405. https://doi.org/10.1029/2007JB005008

Niemeijer, A. R., Spiers, C. J., & Bos, B. (2002). Compaction creep of quartz sand at 400–600°C: Experimental evidence for dissolution controlled pressure solution. *Earth and Planetary Science Letters*, *195*(3–4), 261–275. https://doi.org/10.1016/S0012-821X(01)00593-3

Niemeijer, A. R., & Vissers, R. L. M. (2014). Earthquake rupture propagation inferred from the spatial distribution of fault rock frictional properties. *Earth and Planetary Science Letters*, *396*, 154–164. https://doi.org/10.1016/j.epsl.2014.04.010

Noda, H. (2008). Frictional constitutive law at intermediate slip rates accounting for flash heating and thermally activated slip process. *Journal of Geophysical Research*, *113*, B09302. https://doi.org/10.1029/2007JB005406

Ohnaka, M. (2003). A constitutive scaling law and a unified comprehension for frictional slip failure, shear fracture of intact rock, and earthquake rupture. *Journal of Geophysical Research*, *108*(B2), 2080. https://doi.org/10.1029/2000JB000123

Okubo, P. G., & Dieterich, J. H. (1984). Effects of physical fault properties on frictional instabilities produced on simulated faults. *Journal of Geophysical Research*, *89*(B7), 5817–5827. https://doi.org/10.1029/JB089iB07p05817

Palmer, A. C., & Rice, J. R. (1973). The growth of slip surfaces in the progressive failure of over-consolidated clay. *Proceedings of the Royal Society of London. Series A: Mathematical and Physical Sciences*, *332*(1591), 527–548. https://doi.org/10.1098/rspa.1973.0040

Paterson, M. S. (1995). A theory for granular flow accommodated by material transfer via an intergranular fluid. *Tectonophysics*, *245*(3–4), 135–151. https://doi.org/10.1016/0040-1951(94)00231-W

Paterson, M. S., & Wong, T.-F. (2005). *Experimental rock deformation—The brittle field* (2nd ed.). Berlin: Springer.

Persson, B. N. J. (1998). *Sliding friction: Physical principles and applications*. Heidelberg: Springer. https://doi.org/10.1007/978-3-662-03646-4

Pluymakers, A. M. H., & Spiers, C. J. (2014). Compaction creep of simulated anhydrite fault gouge by pressure solution: Theory v. experiments and implications for fault sealing. In D. R. Faulkner, E. Mariani, & J. Mecklenburgh (Eds.), *Rock deformation from field, experiments and theory: A volume in Honour of Ernie Rutter*, *Special Publications* (Vol. 409, pp. 107–124). Geological Society, London. https://doi.org/10.1144/SP409.6

Poirier, J.-P. (1985). *Creep of crystals* (p. 260). New York: Cambridge University Press. https://doi.org/10.1017/CBO9780511564451

Putelat, T., Dawes, J. H. P., & Willis, J. R. (2007). Sliding interactions of two frictional interfaces. *Journal of the Mechanics and Physics of Solids*, *55*(10), 2073–2105.

Putelat, T., Dawes, J., & Willis, J. (2011). On the microphysical foundations of rate and-state friction. *Journal of the Mechanics and Physics of Solids*, *59*, 1062–1075. https://doi.org/10.1016/j.jmps.2011.02.002

Rathbun, A. P., & Marone, C. (2010). Effect of strain localization on frictional behavior of granular materials. *Journal of Geophysical Research*, *115*, B01204. https://doi.org/10.1029/2009JB006466

Rathbun, A. P., & Marone, C. (2013). Symmetry and the critical slip distance in rate and state friction laws. *Journal of Geophysical Research: Solid Earth*, *118*, 3728–3741. https://doi.org/10.1002/jgrb.50224

Reches, Z., & Lockner, D. A. (2010). Fault weakening and earthquake instability by powder lubrication. *Nature*, *467*, 452–455. https://doi.org/10.1038/nature09348

Renard, F., Park, A., Ortoleva, P., & Gratier, J. P. (1999). A transitional pressure solution model. *Tectonophysics*, *312*(2–4), 97–115. https://doi.org/10.1016/S0040-1951(99)00202-4

Rice, J. R. (1983). Constitutive relations for fault slip and earthquake instabilities. *Pure and Applied Geophysics*, *121*(3), 443–475. https://doi.org/10.1007/BF02590151

Rice, J. R., Lapusta, N., & Ranjith, K. (2001). Rate and state dependent friction and the stability of sliding between elastically deformable solids. *Journal of the Mechanics and Physics of Solids*, *49*(9), 1865–1898. https://doi.org/10.1016/S0022-5096(01)00042-4

Rice, J. R., & Ruina, A. L. (1983). Stability of steady frictional slipping. *Journal of Applied Mechanics*, *50*(2), 343–349. https://doi.org/10.1115/1.3167042

Rice, J. R., & Tse, S. T. (1986). Dynamic motion of a single degree of freedom system following a rate and state dependent friction law. *Journal of Geophysical Research*, *91*(B1), 521–530. https://doi.org/10.1029/JB091iB01p00521

Richardson, E., & Jordan, T. H. (2002). Seismicity in deep gold mines of South Africa: Implications for tectonic earthquakes. *Bulletin of the Seismological Society of America*, *92*(5), 1776–1782.

Richardson, E., & Marone, C. (1999). Effect of normal stress vibrations on frictional healing. *Journal of Geophysical Research*, *104*(B12), 28,859–28,878. https://doi.org/10.1029/1999JB900320

Rubin, A. M., & Ampuero, J.-P. (2005). Earthquake nucleation on (aging) rate and state faults. *Journal of Geophysical Research*, *110*, B11312. https://doi/org/10.1029/2005JB003686

Ruina, A. (1983). Slip instability and state variable laws. *Journal of Geophysical Research*, *88*(B12), 10,359–10,370. https://doi.org/10.1029/JB088iB12p10359

Sammis, C. G., & Biegel, R. L. (1989). Fractals, fault-gouge and friction. *Pure and Applied Geophysics*, *131*(1–2), 255–271. https://doi.org/10.1007/BF00874490

Samuelson, J., Elsworth, D., & Marone, C. (2011). Influence of dilatancy on the frictional constitutive behavior of a saturated fault zone under a variety of drainage conditions. *Journal of Geophysical Research*, *116*, B10406. https://doi.org/10.1029/2011JB008556

Scholz, C. H. (2002). *The mechanics of earthquakes and faulting* (p. 471). Cambridge, UK: Cambridge University Press. https://doi.org/10.1017/CBO9780511818516

Scott, G. D., & Kilgour, D. M. (1969). The density of random close packing of spheres. *Journal of Physics D: Applied Physics*, *2*(6), 863–866. https://doi.org/10.1088/0022-3727/2/6/311

Segall, P. (2010). *Earthquake and volcano deformation* (424 pp.). Princeton, NJ: Princeton University Press.

Segall, P., & Rice, J. R. (1995). Dilatancy, compaction, and slip instability of a fluid-infiltrated fault. *Journal of Geophysical Research*, *100*(B11), 22,155–22,171. https://doi.org/10.1029/95JB02403

Segall, P., Rubin, A. M., Bradley, A. M., & Rice, J. R. (2010). Dilatant strengthening as a mechanism for slow slip events. *Journal of Geophysical Research*, *115*, B12305. https://doi.org/10.1029/2010JB007449

Shibazaki, B., & Shimamoto, T. (2007). Modelling of short-interval silent slip events in deeper subduction interfaces considering the frictional properties at the unstable-stable transition regime. *Geophysical Journal International*, *171*(1), 191–205. https://doi.org/10.1111/j.1365-246X.2007.03434.x

Shimamoto, T. (1986). Transition between frictional slip and ductile flow for halite shear zones at room temperature. *Science*, *231*(4739), 711–714. https://doi.org/10.1126/science.231.4739.711

Sleep, N. H. (1995). Ductile creep, compaction, and rate and state dependent friction within major fault zones. *Journal of Geophysical Research*, *100*(B7), 13,065–13,080. https://doi.org/10.1029/94JB03340

Sleep, N. H. (1997). Application of a unified rate and state friction theory to the mechanics of fault zones with strain localization. *Journal of Geophysical Research*, *102*(B2), 2875–2895. https://doi.org/10.1029/96JB03410

Sleep, N. H. (2005). Physical basis of evolution laws for rate and state friction. *Geochemistry, Geophysics, Geosystems*, *6*, Q11008. https://doi.org/10.1029/2005GC000991

Sleep, N. H., Richardson, E., & Marone, C. (2000). Physics of strain localization in synthetic fault gouge. *Journal of Geophysical Research*, *105*(B11), 25,875–25,890. https://doi.org/10.1029/2000JB900288

Spiers, C. J., De Meer, S., Niemeijer, A. R., & Zhang, X. (2004). Kinetics of rock deformation by pressure solution and the role of thin aqueous films. In S. Nakashima, et al. (Eds.), *Physicochemistry of water in geological and biological systems* (pp. 129–158). Tokyo: University Academic Press.

Stesky, R. M. (1977). Mechanisms of high temperature frictional sliding in westely granite. *Canadian Journal of Earth Sciences*, *15*, 361–375.

Takahashi, M., van den Ende, M. P. A., Niemeijer, A. R., & Spiers, C. J. (2017). Shear localization in a mature mylonitic rock analog during fast slip. *Geochemistry, Geophysics, Geosystems*, *18*(2), 513–530. https://doi.org/10.1002/2016GC006687

Tse, S. T., & Rice, J. R. (1986). Crustal earthquake instability in relation to the depth variation of frictional slip properties. *Journal of Geophysical Research*, *91*(B9), 9452–9472. https://doi.org/10.1029/JB091iB09p09452

Tsutsumi, A., & Shimamoto, T. (1997). High-velocity frictional properties of gabbro. *Geophysical Research Letters*, *24*(6), 699–702. https://doi.org/10.1029/97GL00503

Van den Ende, M., Niemeijer, A. R., & Spiers, C. J. (2015). A microphysical interpretation of the rate-and-state friction direct effect: Implications for the seismic cycle, Geophysical Research Abstracts, 17, EGU2015-10402, EGU General Assembly.

Verberne, B. A., Niemeijer, A. R., De Bresser, J. H. P., & Spiers, C. J. (2015). Mechanical behavior and microstructure of simulated calcite fault gouge sheared at 20–600°C: Implications for natural faults in limestones. *Journal of Geophysical Research: Solid Earth*, *120*, 8169–8196. https://doi.org/10.1002/2015JB012292

Verberne, B. A., Spiers, C. J., Niemeijer, A. R., De Bresser, J. H. P., De Winter, D. A. M., & Plümper, O. (2013). Frictional properties and microstructure of calcite-rich fault gouges sheared at sub-seismic sliding velocities. *Pure and Applied Geophysics*, *171*, 2617–2640.

Weeks, J. D. (1993). Constitutive laws for high-velocity frictional sliding and their influence on stress drop during unstable slip. *Journal of Geophysical Research*, *98*(B10), 17,637–17,648. https://doi.org/10.1029/93JB00356

Yasuda, T., Yagi, Y., Mikumo, T., & Miyatake, T. (2005). A comparison between Dc'-values obtained from a dynamic rupture model and waveform inversion. *Geophysical Research Letters*, *32*, L14316. https://doi.org/10.1029/2005GL023114

Zhang, L., & He, C. (2016). Frictional properties of phyllosilicate-rich mylonite and conditions for the brittle-ductile transition. *Journal of Geophysical Research: Solid Earth*, *121*, 3017–3047. https://doi.org/10.1002/2015JB012489

Zhang, X., Spiers, C. J., & Peach, C. J. (2010). Compaction creep of wet granular calcite by pressure solution at 28°C to 150°C. *Journal of Geophysical Research*, *115*, B09217. https://doi.org/10.1029/2008JB005853